Three Types of Positive Indian Ocean Dipoles and Their Relationships with the South Asian Summer Monsoon

Jilan Jiang,[a,b] Yimin Liu,[a,b] Jiangyu Mao,[a] Jianping Li,[c,d] Shuwen Zhao,[a,b] and Yongqiang Yu[a,b]

[a] *State Key Laboratory of Numerical Modeling for Atmospheric Sciences and Geophysical Fluid Dynamics, Institute of Atmospheric Physics, Chinese Academy of Sciences, Beijing, China*
[b] *University of Chinese Academy of Sciences, Beijing, China*
[c] *Frontiers Science Center for Deep Ocean Multispheres and Earth System, Key Laboratory of Physical Oceanography, Institute for Advanced Ocean Studies, Ocean University of China, Qingdao, China*
[d] *Laboratory for Ocean Dynamics and Climate, Pilot Qingdao National Laboratory for Marine Science and Technology, Qingdao, China*

ABSTRACT: The relationship between the Indian Ocean dipole (IOD) and the South Asian summer monsoon (SASM), which remains a subject of controversy, was investigated using data analyses and numerical experiments. We categorized IOD events according to their sea surface temperature anomaly (SSTA) pattern: type W and type E are associated with stronger SSTA amplitudes in the western and eastern poles of the IOD, respectively, while type C has comparable SSTA amplitudes in both poles during boreal autumn. Type W is associated with a weak SASM from May to summer, which contributes to substantial warming of the western pole in autumn; the east–west SST gradient linked to the warming of the western pole causes weak southeasterly wind anomalies off Sumatra and feeble and cold SSTAs in the eastern pole during the mature phase. Type E is associated with a strong SASM and feeble warming of the western pole; interaction between the strong SASM and cold SSTAs in the eastern pole in summer results in strong southeasterly wind anomalies off Sumatra and substantial cooling of the eastern pole during the mature phase. For type C, warming of the western pole and cooling of the eastern pole develop synchronously without apparent SASM anomalies and reach comparable intensities during the mature phase. Observations and numerical simulation results both indicate the role of disparate SASM anomalies in modulating SSTA patterns during the development of positive IODs. Warming of the tropical Indian Ocean becomes established in the winter and spring following type W and type C IODs but not following type E events.

KEYWORDS: Atmosphere; Ocean; Indian Ocean; Atmosphere-ocean interaction; Atmospheric circulation; Ocean circulation; Ocean dynamics; Monsoons; Climate variability; Heat budgets/fluxes

1. Introduction

The Indian Ocean dipole (IOD) is one of the dominant interannual variabilities in the tropical Indian Ocean (TIO), with a positive (negative) IOD being characterized by warm (cold) SSTAs in the western TIO and cold (warm) SSTAs in the southeastern TIO (Saji et al. 1999; Webster et al. 1999). IOD events strongly influence the climate over the Indian Ocean and surrounding countries, and even on remote regions, for example, Europe, northeast Asia, and North and South America (Birkett et al. 1999; Latif et al. 1999; Webster et al. 1999; Saji and Yamagata 2003; Cai et al. 2014; Nur'utami and Hidayat 2016; Lestari et al. 2018). Moreover, IOD events also contribute to variabilities in oceanic processes, such as the Indonesian throughflow, the equatorial undercurrent of the Indian Ocean, and the eastern Indian Ocean upwelling (Chen et al. 2015, 2016a,b; Liu et al. 2015). Therefore,

comprehensive investigation of the IOD formation and development mechanisms is vital.

Most studies conclude that IOD events have been remotely forced by El Niño–Southern Oscillation (ENSO) in the tropical Pacific Ocean (Xie et al. 2002; Annamalai et al. 2003; Fischer et al. 2005; Zhang et al. 2015; Fan et al. 2017; L. Liu et al. 2017; Stuecker et al. 2017). However, some IOD events, for example, the event in 1961, could have been the result of local air–sea interactions in the TIO (Saji et al. 1999; Webster et al. 1999; Ashok et al. 2003; Li et al. 2003; Rao and Behera 2005; Wang et al. 2016), and some analyses of modeling results and observational data indicate that the influence of ENSO might not be a necessary trigger for IOD events (Fischer et al. 2005; Drbohlav et al. 2007).

Many studies have revealed the crucial role of the Asian summer monsoon in IOD formation (Loschnigg et al. 2003; Drbohlav et al. 2007; Huang and Shukla 2007; Krishnan and Swapna 2009). Krishnan and Swapna (2009) emphasized that enhanced summer monsoon meridional circulations during positive IOD events further intensify the IOD. Early onset of the Bay of Bengal summer monsoon might trigger a positive IOD, independent of the influence of El Niño, through inducing an equatorial easterly wind anomaly (Sun et al. 2015). Recent studies indicated that a strong South China Sea summer monsoon could promote development of positive IOD events (Y. Z. Zhang et al. 2018 2019). Referring to the

---

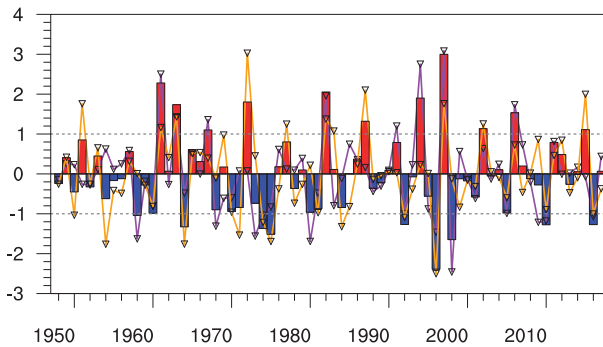

Corresponding author: Yimin Liu, lym@lasg.iap.ac.cn

FIG. 1. Standardized time series of the SON-averaged DMI (bars), EDMI (multiplied by −1.0, purple line), and WDMI (orange line) during 1948–2017. Dashed lines indicate ±1 standard deviation.

influence of the South Asian summer monsoon (SASM) on the IOD, Li et al. (2003) proposed that a strong Indian summer monsoon might exert negative feedback on the IOD. Loschnigg et al. (2003) highlighted that a reduced SASM circulation contributes to development of a positive dipole through reducing (enhancing) upwelling in the western (eastern) equatorial Indian Ocean. However, Drbohlav et al. (2007) indicated that a pattern of monsoon-like flow in non–El Niño years promotes a positive IOD by increasing the westerly and southeasterly wind over the northwestern and southeastern Indian Ocean, respectively. To understand this controversy, we analyzed the latest available data and found no significant correlation between the SASM and either the summer IOD or the autumn IOD. Cherchi et al. (2021) also indicated that the coupling and feedback processes between the SASM and the IOD lack a comprehensive understanding. Therefore, the relationship between the SASM and the IOD needs further investigation, especially with regard to the influence of the SASM on the IOD.

Different types of IOD have been reported in previous studies. Classification of IODs has been based either on the triggering mechanism—mechanisms can be locked into or independent of ENSO (Fischer et al. 2005; Drbohlav et al. 2007; Hong et al. 2008b; Guo et al. 2015) or on the influence of different types of ENSO on IOD occurrence (Wang and Wang 2014; Zhang et al. 2015; Fan et al. 2017). Du et al. (2013) also divided IOD events into three types according to the peak time and duration of events; Anil et al. (2016) further examined the influence of these different types of IODs on Indian summer monsoon rainfall. Endo and Tozuka (2016) found that the western pole of IOD is not always covered entirely by positive SSTAs, and consequently classified IOD episodes as canonical IOD and IOD Modoki events.

It is important to understand differences between the SSTA amplitude of the IOD eastern and western pole, because the impact of different types of IODs on the climate of surrounding countries is saliently disparate, especially in terms of precipitation patterns (Fig. S1 in the online supplemental material). Sun et al. (2014) classified IODs according to their SSTA patterns: when the SSTA amplitude of the

eastern pole exceeds twice that of the western pole during the IOD mature phase, the IOD is classified as an asymmetric IOD; otherwise, it is classified as a symmetric IOD. Recently, Cai et al. (2020) classified positive IODs according to their spatial patterns and dynamics: positive IODs are classified as strong when cold SSTAs of the eastern pole are dominant and are classified as moderate when warm SSTAs of the western pole are dominant. On the basis of differences between the SSTA amplitude of the eastern and western pole, we considered that IODs should be comprehensively grouped into three types (Fig. 1).

In accordance with the criteria of Sun et al. (2014), we defined type W IODs as those in which the SSTA amplitude in the western TIO exceeds twice that in the southeastern TIO; type E IODs are those in which the SSTA amplitude in the southeastern TIO exceeds twice that in the western TIO; type C IODs have comparable SSTA amplitudes in the two poles. Therefore, the objectives of the present study are to investigate features and dynamics of the evolution of these three types of IODs, examine linkages of three types of positive IODs with the SASM, and identify the disparate SSTA development in the Indian Ocean in the winter and spring following IOD events.

Section 2 presents the data, method, and model used in the study. Three types of IOD events are described in section 3. In section 4, we present features of the monsoon circulation, subsurface variations, and the role of the SASM in the development of three types of positive IODs based on observations and numerical simulations. In section 5, we examine the oceanic mixed layer heat budget. In section 6, we discuss the role of El Niño on IODs and the development of SSTAs in the TIO following three types of IOD events. Finally, a summary is given in section 7.

2. Data, method, and model

a. Data

We used SST data from the Hadley Centre Sea Ice and Sea Surface Temperature dataset, version 1.1 (HADISST1; 1948–2017), which has a 1° × 1° horizontal resolution (Rayner et al. 2003). The seawater potential temperature and sea surface height (SSH) were derived from the European Centre for Medium-Range Weather Forecasts (ECMWF) Ocean Reanalysis System 4 (ORAS4) dataset with a 1° × 1° horizontal resolution for the period of 1958–2017 (Balmaseda et al. 2013). SSH derived from the Simple Ocean Data Assimilation (SODA, version 2.2.4) reanalysis dataset with 0.5° × 0.5° horizontal resolution for the period of 1948–2008 (Carton and Giese 2008) was used as comparative analysis. Wind fields and geopotential height with 2.5° × 2.5° horizontal resolution, for the period 1948–2017 were obtained from the National Centers for Environmental Prediction (NCEP) and National Center for Atmospheric Research (NCAR) reanalysis dataset (Kalnay et al. 1996). Outgoing longwave radiation (OLR) data with 2.5° × 2.5° horizontal resolution (1979–2017) were acquired from the National Oceanic and Atmospheric Administration (NOAA; Liebmann and Smith 1996).

Precipitation products were derived from the Japanese 55-year Reanalysis (JRA-55) dataset (1958–2015) with $1.25° \times 1.25°$ horizontal resolution (Kobayashi et al. 2015). All the above datasets are monthly means.

Pentad potential temperature, zonal and meridional currents, and vertical velocities were taken from the NCEP Global Ocean Data Assimilation System (GODAS) at 40 levels (Behringer and Xue 2004), and the daily surface heat flux data were derived from the newly developed TropFlux products (Kumar et al. 2012, 2013), all for 1980–2017. Daily variables of TropFlux were converted into pentad datasets. These GODAS variables were interpolated to $1° \times 1°$ horizontal resolution for convenient analysis in the mixed layer temperature (MLT) tendency equation, following Mao and Wang (2018). A linear trend and the monthly (pentad) mean climatology were removed from each monthly (pentad) dataset. To extract the interannual signal, a 3–108-month bandpass filter was applied to all variables (Guo et al. 2015).

b. Method

The dipole mode index (DMI), which measures the strength of IOD, was defined as the difference between area-averaged SSTAs in the western pole (10°S–10°N, 50°–70°E; WDMI) and the eastern pole (10°S–0°, 90°–110°E; EDMI; Saji et al. 1999). A September–November (SON)-averaged DMI that is greater than 1 standard deviation indicates the occurrence of an IOD event. The Indian Ocean basin mode index was defined as area-averaged SSTAs in the TIO (20°S–20°N, 40°–100°E; Guo et al. 2018). The Niño-3.4 index was calculated from area-averaged SSTAs in the Niño-3.4 region (5°N–5°S, 120°–170°W), and an El Niño occurs if the 5-month running mean of the Niño-3.4 index exceeds 0.4°C for 6 months or more (Trenberth 1997).

The SASM index (SASMI) was defined as an area-averaged dynamical normalized seasonality wind at the 850-hPa wind field in June–August (JJA) within the South Asian domain (5°–22.5°N, 35°–97.5°E; Li and Zeng 2002). The dynamical normalized seasonality index was given by the following:

$$\sigma_{m,n} = \frac{\|\bar{V}_1 - V_{m,n}\|}{\|\bar{V}\|} - 2, \tag{1}$$

where $\bar{V}_1$ and $\bar{V}$ are the January climatological wind vector and the mean of January and July climatological wind vectors, respectively, and $V_{m,n}$ is the monthly wind vector for the mth month of the nth year.

The mixed layer heat budget equation (Li et al. 2002; He et al. 2019) can be expressed as follows:

$$\frac{\overline{\partial T}}{\partial t} = \frac{Q_{net} - Q_p}{\rho C_p h} - \overline{u \frac{\partial T}{\partial x}} - \overline{v \frac{\partial T}{\partial y}} - \overline{w \frac{\partial T}{\partial z}} + R, \tag{2}$$

where $\overline{()} = (1/h) \int_{-h}^{0} dz$ represents the vertical means over the mixed layer; h represents the mixed layer depth, which is approximately 45 m in the Indian Ocean (Du et al. 2005; He et al. 2019); u, v, and w represent the zonal current,

meridional current, and vertical current, respectively; Q_{net} represents the downward net surface heat flux, including the net downward shortwave radiation flux, longwave radiation flux, latent heat flux, and sensible heat flux; and Q_p represents the shortwave penetration through the mixed layer depth. The solar radiation penetration parameterization scheme is as follows (Paulson and Simpson 1977):

$$Q_p = SW \times [r \times e^{-h/L_1} + (1 - r) \times e^{-h/L_2}], \tag{3}$$

where SW indicates the downward shortwave radiation at the sea surface, $r = 0.67$, $L_1 = 1$, and $L_2 = 17$ (Dong et al. 2007). The density of seawater is 1026 kg m^{-3}, and its specific heat is 3986 J kg^{-1} K^{-1}. R in (2) represents the residual term that includes various components such as unresolved subgrid-scale turbulence and eddy heat flux (Du et al. 2005).

The statistical significance of composites was tested using two-tailed Student's t tests. Special care was taken to interpret results from the composite analysis because of the small number of cases in each IOD type. The composite analysis, linear baroclinic model (LBM) experiments, ocean general circulation model experiments, and ocean mixed layer heat budget diagnoses all will be conducted to indicate the reliability of results.

c. Model

In this study, we used two models. One is the LBM (Watanabe and Kimoto 2000; Watanabe and Jin 2002). The NCEP1 reanalysis data from the period of June–August (summer) 1979–2014 were used as model input. We performed a 30-day integration for each experiment with fixed diabatic heating forcing. Model results from days 15 to 30 were averaged and examined in this study.

Numerical experiments of IOD events also were conducted using LICOM3, which is an oceanic general circulation model developed by the State Key Laboratory of Numerical Modeling for Atmospheric Sciences and Geophysical Fluid Dynamics (LASG) of the Institute of Atmospheric Physics (IAP) of the Chinese Academy of Sciences (CAS). Detailed descriptions of LASG/IAP LICOM3 can be found in Lin et al. (2020). We conducted sensitivity experiments, which were based on the Ocean Model Intercomparison Project (OMIP) experiment in phase 6 of the Coupled Model Intercomparison Projects (CMIP6); Coordinated Ocean–Ice Reference Experiments, phase II (CORE-II), data derived from NCEP–NCAR reanalysis for 1948–2009 (Large and Yeager 2004) were used as the forcing data.

3. Classification of IOD events

a. Three types of IODs

Following the classification criteria described in section 1, we identified approximately 11 (9) positive (negative) IOD events between 1948 and 2017 (Table 1); our results are largely consistent with findings of previous studies (Saji and Yamagata 2003; Du et al. 2013; Endo and Tozuka 2016). Figure 1 shows the strength of SON-averaged DMI, WDMI, and

TABLE 1. Years with type W, type E, type C, and positive and negative IOD events.

Types	Positive IODs	Negative IODs
Type W (stronger in western pole)	1972[a], 1987[a], 2015[a]	1964[a]
Type E (stronger in eastern pole)	1961, 1967, 1994[a], 2006[a]	1958, 1998[a]
Type C (symmetric)	1963[a], 1982[a], 1997[a], 2002[a]	1974, 1975[a], 1992, 1996, 2010[a], 2016[a]

[a] Positive (negative) IOD event co-occurring with El Niño (La Niña).

EDMI (multiplied by −1.0). Type W positive (negative) IOD events, in which the amplitude of WDMI is at least twice that of the EDMI, occurred in 1972, 1987, and 2015 (1964). Type E positive (negative) IOD events, in which the amplitude of EDMI is at least twice that of the WDMI, occurred in 1961, 1967, 1994, and 2006 (1958 and 1998). Type C positive (negative) IOD events, in which the amplitude of WDMI is less than twice that of EDMI or the amplitude of EDMI is less than twice that of WDMI, occurred in 1963, 1982, 1997, and 2002 (1974, 1975, 1992, 1996, 2010, and 2016).

There was significant asymmetry between positive and negative phases of three types of IODs (not shown). Previous studies emphasized the prominence of the asymmetry of SSTA amplitude between IOD positive and negative phases (Hong et al. 2008a,c; Ogata et al. 2013; L. Y. Zhang et al. 2018), and that the amplitude of positive IOD events tends to be greater than that of negative IOD events (Cai et al. 2013). For type C, the number of negative IODs exceeds that of positive IODs. As indicated by Hong et al. (2008a,c), the SST in the eastern TIO is warm with more active ocean–atmosphere interaction, which determines that the SST cooling in the IOD eastern pole is much easier and stronger than the warming. The asymmetric thermocline feedback induced by the deep mean thermocline in the southeastern TIO, in which

SST is more sensitive to shoaling than the deepening of the thermocline, also contributes to the domination of cooling over warming (Ogata et al. 2013; Cai et al. 2013). Such asymmetry causes more negative IODs in the type C category. Moreover, Hong et al. (2008b) suggested that positive and negative IOD events differ in their evolution and structures. Thus, we separated positive IODs from negative IODs, and in this paper, only focus on positive IODs.

b. Temporal features of the evolution of three types of positive IODs

The temporal evolution of WDMI and EDMI differs markedly among three types of IODs (Fig. 2). For type W IODs, the amplitude of WDMI develops rapidly from spring, and is remarkably greater than that of EDMI after May, especially during the peak of the IOD development phase (Fig. 2a). For type E, the EDMI develops rapidly from late spring, and is remarkably greater than WDMI after June (Fig. 2b). For type C, although SSTAs of two poles develop almost synchronously to reach similar intensity during the mature phase, cooling of the eastern pole is generally greater than warming of the western pole during the entire developing phase, with the event of 2002 being an exception (Fig. 2c). In general, our results indicate that type E and type C IODs are dominated
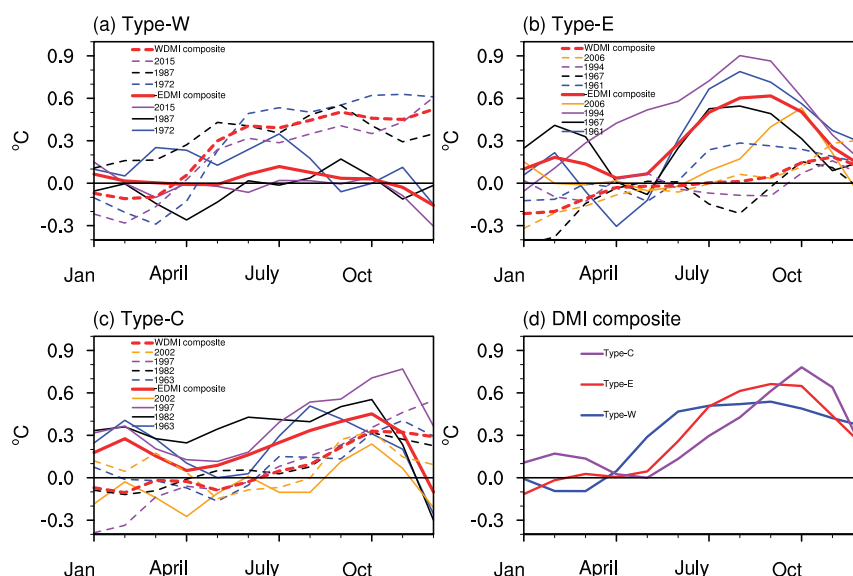

FIG. 2. Evolution of the EDMI (multiplied by −1.0, solid lines), WDMI (dashed lines), and their composite (thick red lines) for positive IODs of (a) type W, (b) type E, (c) type C, and (d) DMI composites for three types of positive IODs. Events in the composite are listed in each panel (unit: °C).

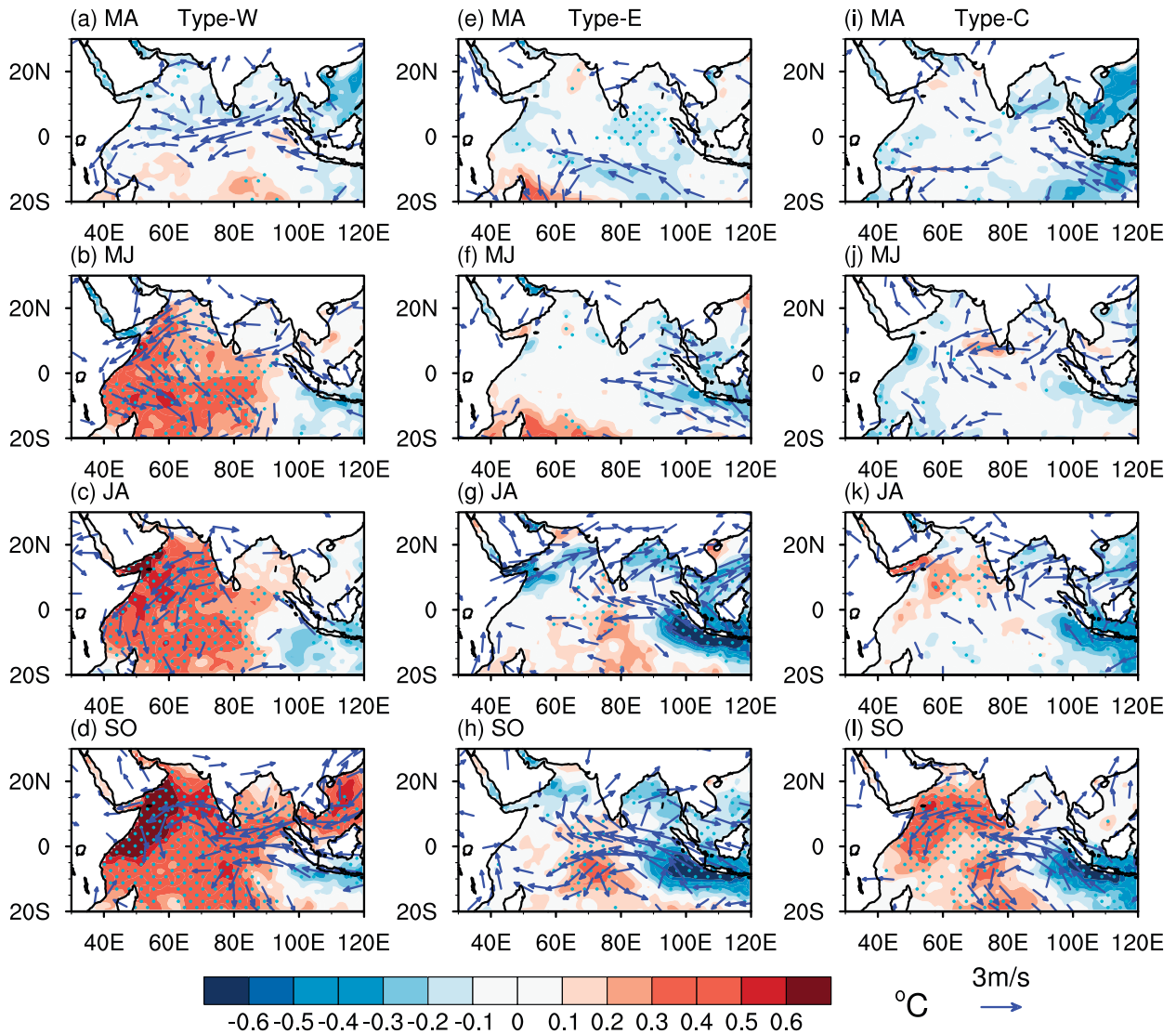FIG. 3. Bimonthly averaged composites of SSTAs (shading, unit: °C) and 925-hPa wind anomalies (vectors, unit: m s^{-1}) for positive IODs of (left) type W, (center) type E, and (right) type C: (a),(e),(i) March–April (MA); (b),(f),(j) May–June (MJ); (c),(g),(k) July–August (JA); (d),(h),(l) September–October (SO). Cyan stippling indicates the 90% confidence level. Only wind vectors that are significant at the 90% confidence level are shown.

by cold SSTAs in the southeastern TIO and are consistent with previous studies (Webster et al. 1999; Luo et al. 2010; Du et al. 2013). Figure 2d shows that a type E IOD is stronger than a type W IOD. Of the three types, a type C IOD is the last to start its development phase but is the strongest during its mature phase.

4. Contrasts among three types of positive IODs

a. Monsoon circulation and SSTAs

To examine the formation processes of three types of positive IODs, we examined bimonthly evolution of SSTAs and 925-hPa wind anomalies (Fig. 3). Composite results

derived using 1 standard deviation of the SON-averaged DMI as the threshold to define IOD occurrence are in close agreement with results derived using a 0.75 or 1.5 standard deviation threshold (not shown). For type W IODs (Figs. 3a–d), easterly anomalies dominate the equatorial Indian Ocean and northern Indian Ocean during March–April (Fig. 3a). Such anomalous easterlies tend to drive warm water to accumulate westward, facilitating positive SSTAs. Significant positive SSTAs appear in the western TIO during May–June, accompanied by anomalous easterlies (westerlies) over the region north (south) of the equator (Fig. 3b). Moreover, as May–June is the period of onset of southwesterly monsoon over the Indian subcontinent, anomalous easterlies there coincide with delayed
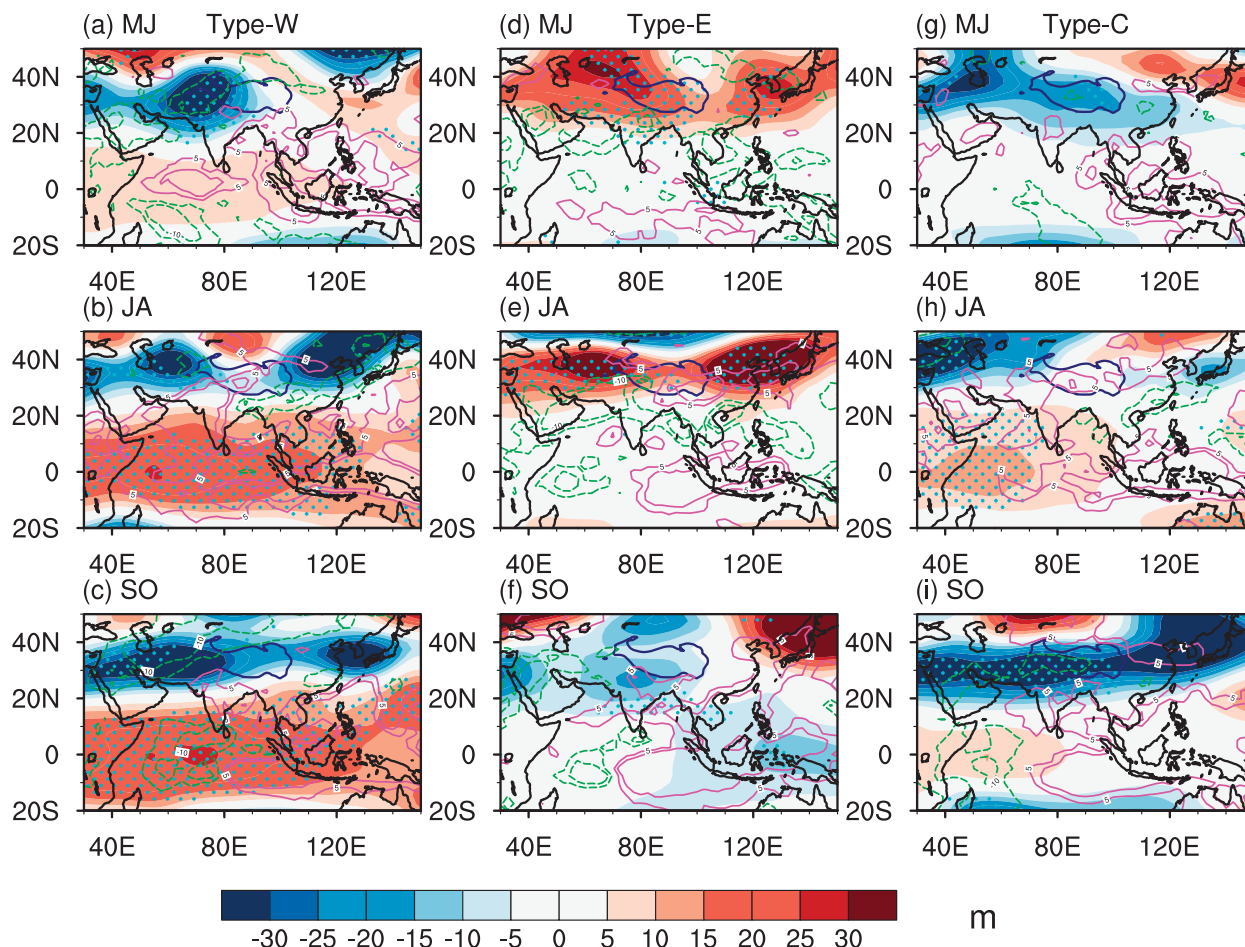
FIG. 4. Bimonthly averaged composites of 200-hPa geopotential height anomalies (shading, unit: m) and OLR anomalies (contours, units: W m^{-2}) for positive IODs of (left) type W, (center) type E, and (right) type C: (a),(d),(g) MJ; (b),(e),(h) JA; (c),(f),(i) SO. Composites of OLR are for three types of positive IODs during 1979–2017. Green and magenta contours represent negative and positive OLR anomalies, respectively (contour interval: 5 W m^{-2}, zero contour omitted). Cyan stippling indicates the 90% confidence level for composites of 200-hPa geopotential height anomalies. Dark blue contours (3000-m topographic height) indicate the location of the Tibetan Plateau.

onset of the SASM (Yu et al. 2021) and a weakened SASM. Thus, northeasterly wind anomalies are established off East Africa in July–August (Fig. 3c), which weakens wind–evaporation–SST (WES) feedback (Li et al. 2003; Xie and Philander 1994) and coastal upwelling (Murtugudde et al. 2000). Subsequently, positive SSTAs become stronger and reach maxima during September–October as anomalous easterlies intensify, especially over the Arabian Sea (Fig. 3d). There are few signals in the eastern Indian Ocean during spring and summer (Figs. 3a–c). The east–west temperature gradient associated with warming of the western TIO contributes to development of southeasterly wind anomalies off Sumatra in September–October. Correspondingly, cooling of the eastern pole develops there (Fig. 3d). Notably, the SST warming in the western TIO is considerably stronger than the SST cooling in the southeastern TIO after May (Figs. 2a and 3a–d).

In contrast, the development of type E IODs begins from the eastern pole. Southeasterly wind anomalies over the central southern Indian Ocean may contribute to the weak and cold SSTAs in the southeastern Indian Ocean via the offshore flow during March–April (Fig. 3e). Development of southeasterly wind anomalies off Sumatra in May–June strengthens cold SSTAs and suppresses convection in the southeastern TIO via wind–thermocline–SST (Saji et al. 1999) and WES feedback (Fig. 3f). Southeasterly wind anomalies of the eastern pole transport water vapor to India and the Bay of Bengal, contributing to both positive precipitation anomalies (Figs. S1e and S1f) and convection development in spring and summer (contours in Figs. 4d,e). The interaction between the strong SASM and cold SSTAs further cools the eastern pole in July–August, resulting in the SSTA peak in September–October (Figs. 3g,h). In type E IODs, unlike in type W IODs, there are no warm SSTAs off East Africa in summer and autumn owing to enhanced WES feedback and coastal

upwelling resulting from the strong SASM. Accompanying the development of easterly anomalies in the equatorial Indian Ocean, SST warming appears in the central TIO (Figs. 3g,h), similar to the IOD Modoki (Endo and Tozuka 2016).

For type C IODs, weak easterly wind anomalies occur in the northern Indian Ocean during May–June without significant SSTAs in the western Indian Ocean (Fig. 3j). Southeasterly wind anomalies off Sumatra and the coincident significant cold SSTAs begin developing in July–August, that is, later than in type E IODs, and accompany weak westerly wind anomalies over the Indian subcontinent and the Bay of Bengal (Fig. 3k). Meanwhile, warm but weak SSTAs form in the western TIO with the setup of equatorial easterly anomalies (Fig. 3k). There are no prominent summer monsoon anomalies over the western Indian Ocean during the development phase of the IODs (Figs. 3j,k). A typical dipole mode becomes established in September–October, with comparable SSTA amplitudes in the eastern and western poles (Figs. 2c and 3l). Therefore, we conclude that the SST and wind evolution of three types of positive IODs over the western and eastern TIO are remarkably different, which may be related to the strength of the SASM.

Figure 4 illustrates the evolution of the 200-hPa geopotential height anomaly, that is, the South Asian high, and the OLR anomaly associated with three types of positive IODs. The presence of cyclonic circulation anomalies in type W IODs over the southwestern Tibetan Plateau in May–June at 200 hPa (Fig. 4a) and 500 hPa (not shown) signifies a barotropic structure in the mid- to upper troposphere. Previous studies indicated the important role of the variability of the South Asian high in monsoon onset and rainfall variability over South Asia (Ashfaq et al. 2009; Liu et al. 2014; Wei et al. 2019). The weakening of the easterly jet on the southern flank of the South Asian high is unfavorable for the establishment and seasonal development of the SASM (Yu et al. 2021). Yu et al. (2021) also highlighted that an area of high pressure with low-level divergence over India leads to weakening of the cross-equatorial Somali jet near the surface and a delay in the seasonal transition of the SASM, which is consistent with the circulation in type W IODs (Figs. 3a,b, S2a, and S2b). The weakened South Asian high and SASM persist into September–October (Figs. 3b–d and 4a–c). For type E IODs, positive geopotential height anomalies develop along 35°N during May–August (Figs. 4d,e), accompanying with the strong South Asian high. The SASM is established early and is strengthened conspicuously for type E IODs, which contrasts with the situation in type W IODs. Corresponding to insignificant anomalies of the South Asian high and SASM, geopotential height anomalies over the Tibetan Plateau are relatively weak during the development phase of type C IODs (Figs. 4g,h).

Further, in late spring, the South Asian high variability is basically influenced by two systems. One is tropical SSTAs, that is, ENSO (Table 1), SSTAs in the Indian Ocean, and associated convection anomaly in the Indian Ocean and western Pacific (B. Q. Liu et al. 2017). The South Asian high is stronger when the tropical convective heating is enhanced (Liu et al. 2007; B. Q. Liu et al. 2017; Figs. 4d–e). The other is stationary wave activities in midlatitudes, which can generate a baroclinic circulation structure in Iranian Plateau and western

Tibetan Plateau (Cui et al. 2015; Yu et al. 2021; Figs. 4a and S2a). The positive feedback between the weakened South Asian high and monsoon convection sustains the weak SASM and South Asian high during summer in type W IODs (Figs. 3b,c, 4a,b, S2a, and S2b), and vice versa for the strong SASM and South Asian high in type E IODs (Figs. 3f,g, 4d,e, S2d, and S2e).

Marked differences exist in the convection over the western TIO and the South Asian region during May–August among three types of positive IODs. The increased convection in the southwestern Indian Ocean during May–June (Figs. 4a and S1a), which is associated with warm SSTAs, also suppresses the convection over the Indian subcontinent and weakens the SASM. The delay in the SASM seasonal transition and weakened convection in South Asia are coupled with near-surface easterly anomalies in South Asia and a weaker Somali jet in spring and early summer (Figs. 3a,b, 4a, and S2a) that persist in summer (Figs. 3c,b and S2b). For type E IODs, suppressed convection, cold SSTAs, and southeasterly wind anomalies begin in late spring over the eastern pole (Figs. 3f, 4d, and S2d). The stronger easterly shear of the South Asian high and the moisture transport associated with the depressed convection over the southeastern Indian Ocean favor a stronger SASM during May–August, which corresponds to strong convection anomalies over the western TIO and South Asia (Figs. 3f,g, 4d,e, S2d, and S2e). The strong SASM is coupled with the strengthened meridional circulation in the eastern Indian Ocean (not shown), resulting in further cooling of the eastern pole (Fig. 3g). Comparably, convection anomalies over South Asia are weak during spring–summer for type C IODs (Figs. 4g,h). During September–October, convection is significant in the western TIO for both type W and type C IODs owing to the strong SST gradient, whereas it is slightly weaker for type E IODs. The OLR over the southeastern Indian Ocean and Maritime Continent shows suppressed convection during the entire development phase of three types of positive IODs (Fig. 4); positive OLR anomalies are the strongest and the SSTAs are the coldest in the eastern pole of type E IODs. The strong air–sea interaction plays an important role in IOD development. At the western pole, the suppressed convection corresponds to positive SSTAs for type W IODs, and the increased convection corresponds to weak and negative SSTAs for type E IODs during May–August; both phenomena suggest that the atmospheric processes dominate the development of SST patterns there (Figs. 3b,c,f,g, 4a,b,d,e).

Convection is coupled with upper- and lower-tropospheric circulation anomalies, presenting a weakened (strengthened) SASM in type W (type E) IODs. The SASM-related OLR anomalies correspond to the negative or positive heat source, in turn, and such diabatic heating might reduce or reinforce the anomalous circulation (e.g., easterly or westerly anomalies) to enhance SSTAs of type W or type E IODs. The mechanism for this diabatic heating-induced circulation is addressed in section 4c through an analysis of numerical experimental results.

b. Subsurface variations of three types of positive IODs

Oceanic dynamic processes are also important in the IOD development (Murtugudde et al. 2000; Yuan and Liu 2009;

Wang and Yuan 2015; Wang et al. 2016; Effy et al. 2020) and are examined in this section. Following Rao and Behera (2005) and Wang et al. (2016), we used SSH as a proxy of thermocline variability. Large differences in the surface wind anomalies of three types of positive IODs may result in large differences in subsurface temperature and thermocline anomalies (Rao et al. 2002; Rao and Behera 2005; Endo and Tozuka 2016). The longitude–depth pattern of potential temperature anomalies averaged over 10°S–10°N, which are consistent with sections averaged over 5°S–5°N (not shown), and SSH anomalies are shown in Figs. 5 and 6, respectively. SSH anomalies from ORAS4 and SODA data present consistent results (not shown).

For type W IODs, equatorial easterly wind anomalies over the TIO during January–April drive upwelling Kelvin waves to propagate to the eastern Indian Ocean, lifting up the thermocline and contributing to subsurface cooling there (Figs. 5a, 6a, and S3a; Murtugudde et al. 2000; Rao et al. 2002). Meanwhile, as a response to anticyclonic wind stress curl, downwelling Rossby waves associated with the convergence of warm waters in the off-equatorial ocean propagate westward, subsequently deepening the thermocline and promoting the subsurface warming over the western Indian Ocean (Xie et al. 2002; Rao and Behera 2005; Effy et al. 2020). Effy et al. (2020) pointed out that the anomalous subsurface warming helps the western equatorial Indian Ocean to maintain the warmer SST. As indicated by Yuan and Liu (2009), feeble downwelling Kelvin waves reflected at the western boundary provide the negative feedback to the evolution of subsurface processes in the eastern Indian Ocean during May–August (Figs. 5b,c, 6b,c, and S3a). During September–October, the development of local southeasterly wind anomalies off Sumatra also strengthens the subsurface cooling and the thermocline shoaling in the eastern Indian Ocean (Figs. 3d, 5d, and 6d; Murtugudde et al. 2000). Downwelling Rossby waves in the off-equatorial ocean propagate westward, which further deepens the thermocline and enhances warm subsurface temperature anomalies in the western Indian Ocean (Figs. 5d, 6d, S3b, and S3c).

Conversely, for type E IODs, weak westerly wind anomalies generate the eastward propagation of downwelling Kelvin waves over equatorial Indian Ocean and the westward propagation of upwelling Rossby waves over off-equatorial Indian Ocean, contributing to subsurface warming and cooling over the eastern and western Indian Ocean before April, respectively (Figs. 5e, 6e, S3d, S3e, and S3f). The reflected upwelling Kelvin waves at the western boundary propagate eastward to the southeastern Indian Ocean, inducing thermocline shoaling and subsurface cooling during May–June (Figs. 5f, 6f, and S3d). Thermocline shoaling and subsurface cooling in the eastern Indian Ocean continue to strengthen accompanying with the development of southeasterly wind anomalies off Sumatra and easterly wind anomalies over the equatorial Indian Ocean during July–October (Figs. 3g,h, 5g,h, and 6g,h). Downwelling Rossby waves caused by surface wind anomalies in the off-equatorial region propagate westward to the central Indian Ocean during September–October, generating warm subsurface temperature anomalies (Figs. 5h, 6h, and S3d–f).

Weak upwelling Kelvin waves propagate eastward to shoal the thermocline and lead to subsurface cooling over the southeastern Indian Ocean owing to insignificant surface wind anomalies for type C IODs. Subsequently, the reinforced southeasterly wind anomalies off Sumatra intensify the local upwelling and subsurface cooling there (Figs. 5i–l, 6i–l, and S3g). Meanwhile, the westward propagation of downwelling Rossby waves associated with wind anomalies strengthens during September–October, contributing to warming in the western Indian Ocean (Figs. 3k,l, 5k,l, 6k,l, S3h, and S3i). These results suggest that the subsurface temperature and thermocline anomalies associated with three types of positive IODs are observably disparate. Moreover, it is noted that the variation of thermocline does not agree with the SSTA well during March–April (Figs. 3a,e,i, 5a,e,i, and 6a,e,i), suggesting that the oceanic dynamic plays a relatively smaller role during the early development for three types of IODs. The oceanic dynamic strongly contributes to the IOD during its development and mature stages, especially for type E and type C IODs. For type W IODs, the oceanic dynamic contributes less to cold SSTAs of eastern pole during the entire process.

c. Role of the SASM in the development of three types of positive IODs

1) OBSERVATIONS

Three types of positive IODs are related to different SASM circulations. Type W IODs coincide with a weaker SASMI, whereas type E IODs are closely related to a stronger SASMI. The SASM anomaly associated with type C IODs is very weak, except in 2002 when the SASMI is −0.76 (Fig. 7). However, these results are not contradictory, because the weakened SASMI in 2002 is followed by warm SSTAs in the western pole that are larger than cold SSTAs in the eastern pole (Fig. 2c), pointing toward a behavior that is similar to that of a type W IOD.

2) LBM SIMULATION

To investigate the circulation response to a strong or weak SASM-related diabatic heating, LBM experiments were performed. We selected the center location and extent of the negative (positive) heat source on the basis of composites of observed July–August precipitation anomalies for type W (type E) positive IODs (Figs. 8a,d, S1b, and S1f). In the simulation, the negative heat source is centered on 15°N, 75°E; it extends over an elliptical area of 5° latitude × 10° longitude in the region of 10°–20°N, 65°–85°E; the positive heat source is centered on 20°N, 90°E; it extends over an elliptical area of 5° latitude × 20° longitude in the region of 15°–25°N, 70°–110°E (Figs. 8a,d). In the vertical, the area-averaged heating profile has a minimum (maximum) of −0.89 K day^{-1} (0.65 K day^{-1}) at the sigma of 0.54 for negative (positive) condensation heating in the LBM as recorded in observations.

Results presented in Fig. 8 indicate that the SASM plays a vital role in adjusting the SSTA pattern of IODs. The response to a negative heating over South Asia exhibits several remarkable features at low levels of the atmosphere that are conducive to the development of type W IODs
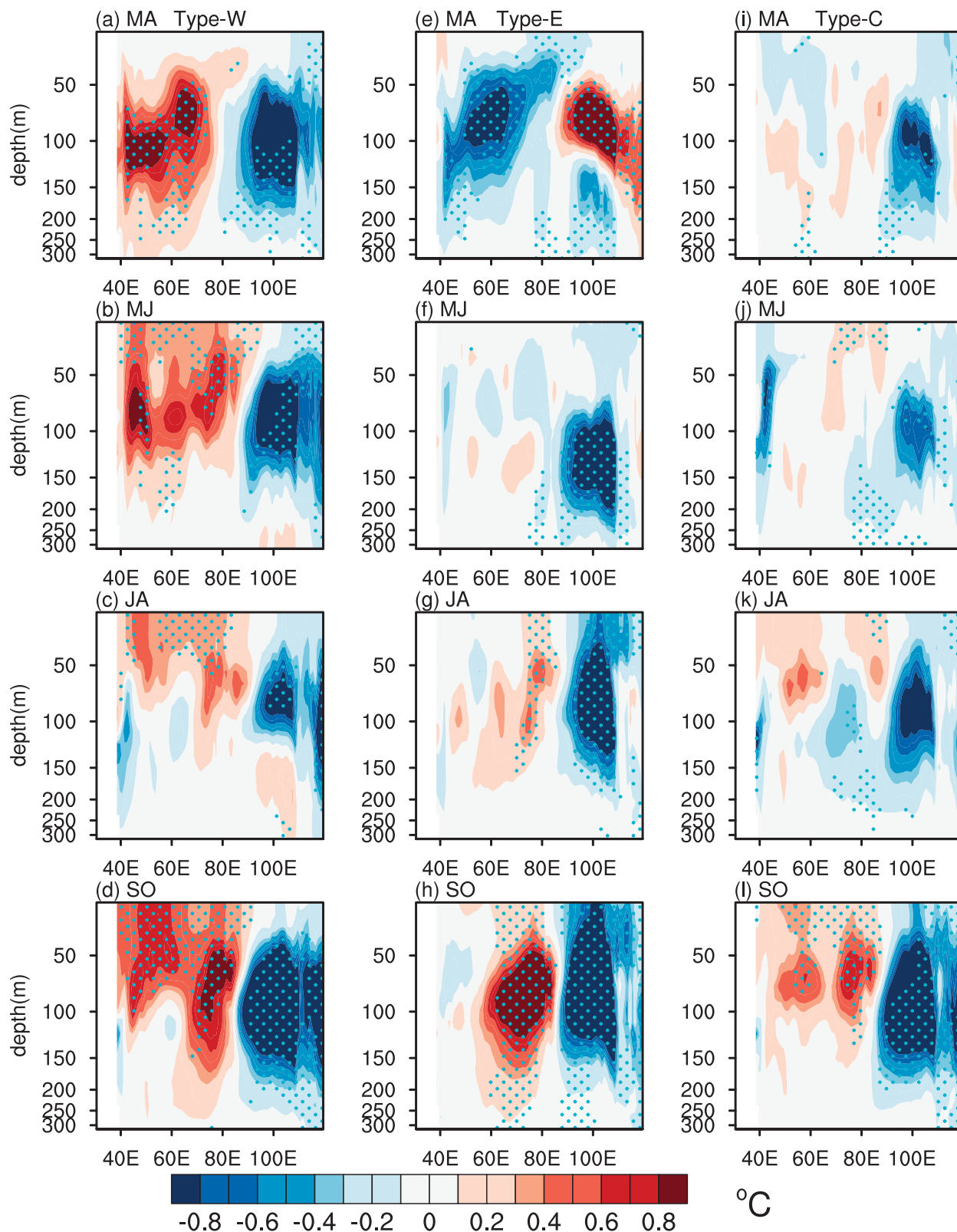
FIG. 5. Bimonthly averaged composites of vertical potential temperature anomalies (unit: °C) calculated as the average over 10°S–10°N for positive IODs of (left) type W, (center) type E, and (right) type C during 1958–2017: (a),(e),(i) MA; (b),(f),(j) MJ; (c),(g),(k) JA; (d),(h),(l) SO. Cyan stippling indicates the 90% confidence level.
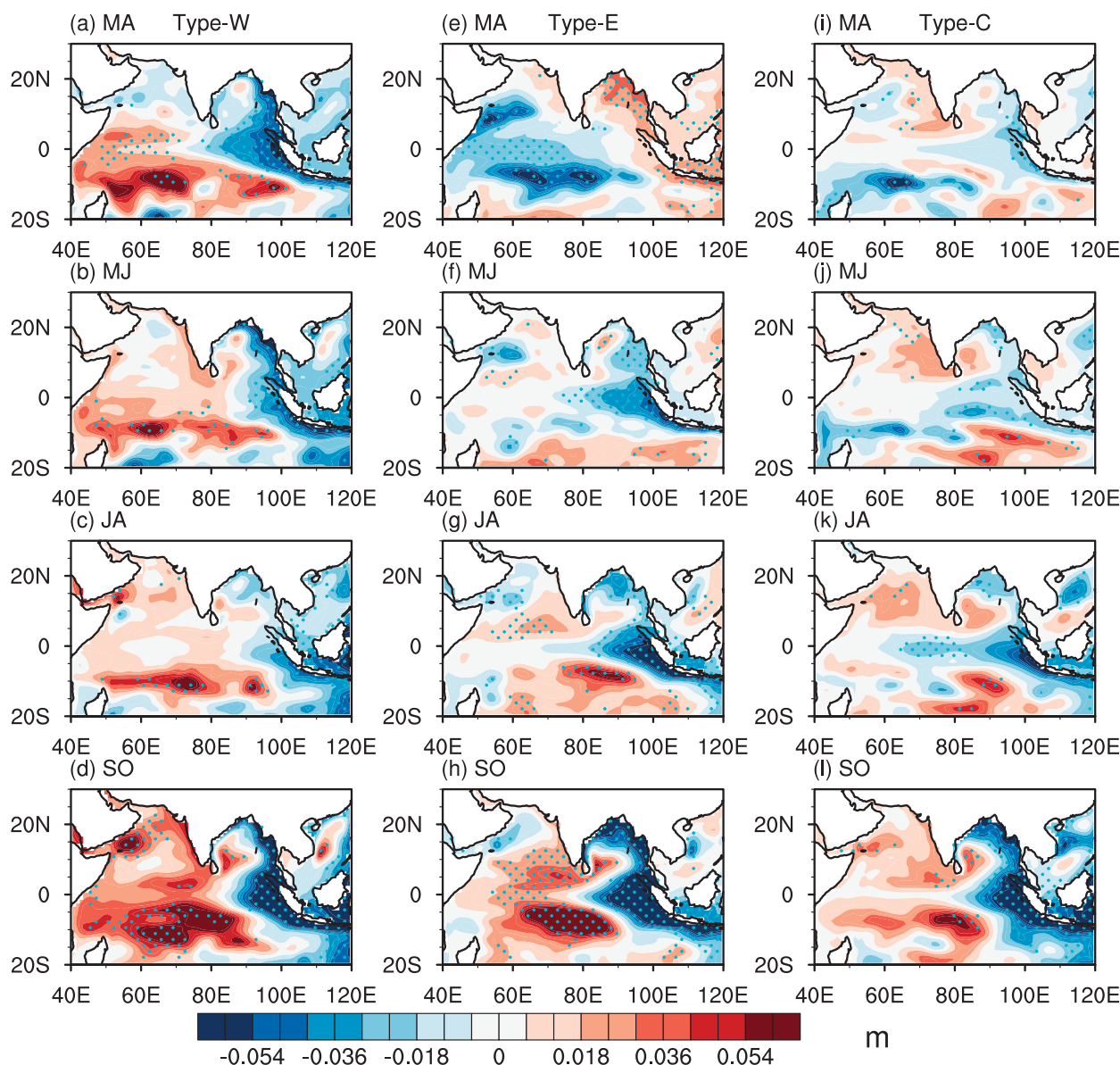
FIG. 6. Bimonthly averaged composites of SSH anomalies (unit: m) for positive IODs of (left) type W, (center) type E, and (right) type C during 1958–2017: (a),(e),(i) MA; (b),(f),(j) MJ; (c),(g),(k) JA; (d),(h),(l) SO. Cyan stippling indicates the 90% confidence level.

(Figs. 8a–c): 1) the evident high pressure that becomes established over the Indian subcontinent and the northwestern Indian Ocean, 2) the easterly wind that forms over southern India and the northwestern Indian Ocean, and 3) the significant northeasterly wind that occurs over the western Indian Ocean and off East Africa, which might facilitate warming of the western pole (Figs. 8b,c).

Conversely, in response to a positive heating associated with a stronger SASM, there is an area of low pressure over the Bay of Bengal and the Indian subcontinent with prominent westerly winds on its southern flank. Corresponding southeasterly winds and easterly winds develop off Sumatra and over the equatorial Indian Ocean, respectively

(Figs. 8d–f). Features of the positive heat source presented here favor the establishment of type E IODs. It should be noted that results from LBM experiments do not exactly match the observation data shown in Fig. 3 because of the lack of feedback in the LBM.

3) OCEANIC GENERAL CIRCULATION MODEL SIMULATION

Numerical experiments were designed and performed using LICOM3 to further investigate the potential role of SASM in the development of positive IODs by considering nonlinear systems. First, we conducted an OMIP experiment from 1948 to 2009, which was an ocean–sea–ice coupled hindcast
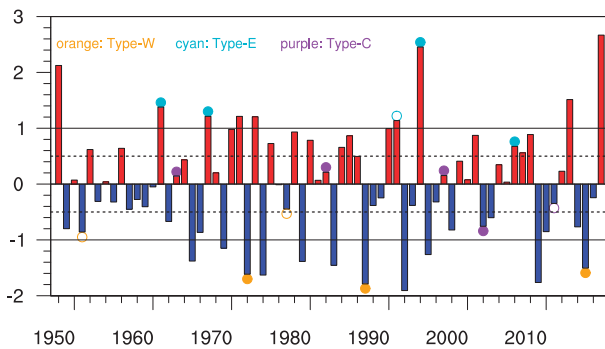
FIG. 7. Standardized time series of JJA-averaged SASMI (bars). Orange, cyan, and purple dots indicate years of positive IODs of type W, type E, and type C, respectively. Orange, cyan, and purple circles indicate years of identifiable positive IODs of type W, type E, and type C when a 0.75 standard deviation of the SON-averaged DMI is used as the threshold to define IOD occurrence, respectively.

simulation forced by CORE-II data (Lin et al. 2020). Type C IODs have comparable SSTA amplitudes in the western and eastern poles in autumn, accompanying with inconspicuous SASM anomalies; thus, four type C positive IOD years from the OMIP experiment—1963, 1982, 1997, or 2002—were selected as the control run (CTL). On the basis of CTL, we conducted two groups of sensitivity experiments in regard to the strong and weak SASM for four cases. For four cases in each group of sensitivity experiment, varying initial conditions were set to the instantaneous field on 1 May from the corresponding CTL. For the WOMIP sensitivity experiment, the surface wind field at 10 m of the CTL from June to August over 20°S–20°N, 40°–120°E was replaced by the composite wind from type W positive IODs; for the EOMIP experiment, the same surface wind field from the CTL was replaced by the composite wind from type E positive IODs. For each case, the oceanic model was integrated to December, and the ensemble mean of four cases is presented in the following section.

The OMIP simulation can satisfactorily reproduce the observed mean states, long-term linear trends, and interannual variabilities (Lin et al. 2020). There is close agreement between observations and simulated positive IODs from the OMIP experiment (not shown). Relative to the climate mean state of OMIP experiments, WOMIP and EOMIP experiment results both show the dipole mode with western pole warming and eastern pole cooling in autumn (Figs. 9a,b). Simultaneously, the warming of western pole in WOMIP experiments is stronger than the cooling of eastern pole, while in EOMIP experiments, the cooling of eastern pole is remarkably stronger than the warming of western pole (Figs. 9a,b).

Then, we examined SST differences between WOMIP and CTL experiments, as well as those between EOMIP and CTL experiments (Figs. 9c,d), and noted the role of SASM in modulating SST patterns during the IOD development. Results from the WOMIP experiment indicate that the weak SASM induces substantial warming in the tropical western Indian Ocean during boreal autumn, especially in the Arabian Sea.

The positive SST differences in the eastern pole suggest that the cooling in WOMIP experiments is weaker than that in CTL experiments, stating that a weak SASM corresponds to the faint cooling of the eastern pole (Figs. 9a,c). Conversely, SST differences between EOMIP and CTL experiments in the eastern pole and the Arabian Sea are negative, which indicates that a strong SASM promotes the cooling of the eastern pole and weakens the warming in the Arabian Sea and off East Africa (Figs. 9b,d). These results demonstrate that a weak (strong) SASM is beneficial for the generation of type W (type E) IODs. Once IODs are initiated, different SASM anomalies can modulate SST patterns and lead to different dipole types, but the SASM anomalies alone are insufficient to trigger SSTA dipole modes.

5. Ocean mixed layer heat budget

a. Closure of the mixed layer heat budget equation

To explore relative impacts of atmospheric thermal forcing and oceanic dynamical processes on the formation of three types of positive IODs, we diagnosed quantitatively the mixed layer heat budget. As displayed in Fig. 10, the forcing, which is defined as the sum of the net surface heat flux and three-dimensional (3D) advections, reproduces features of the MLT tendency for composites of three types of positive IODs. Consistent with Hong et al. (2008b,c), the peaks and evolution of the tendency and forcing match reasonably well. Residuals might have been caused by differences in ocean and surface heat flux data sources, uncertainties in the parameterization, and the use of pentad fields and the $1° \times 1°$ grid (B. Y. Huang et al. 2010). For type W IODs, warm MLT anomalies of the western pole start developing in early spring, but cold MLT anomalies of the eastern pole only become established during the mature phase (Figs. 10a,d). For type E IODs, warm MLT anomalies of the western pole are weak during the entire development phase, but cold MLT anomalies of the eastern pole appear around late spring (Figs. 10b,e). For type C IODs, MLT anomalies of the eastern and western poles both start in the middle of summer (Figs. 10c,f), and are consistent with results shown in Fig. 3.

b. Contributions of components of the mixed layer heat budget equation

1) THE WESTERN POLE

We examined the contribution of each component of the MLT equation to the development of three types of positive IODs. For the western pole of type W IODs, the surface heat flux is significant and positive during May–August (peaking in June–July, Fig. 11a) owing to the positive latent heat flux anomalies and downward shortwave radiation flux anomalies (not shown), and it is consistent with the existence of a weakened SASM (Figs. 3b,c). The continuous positive forcing is well established between May and October, mainly as a result of positive surface heat flux and zonal advection during the summer monsoon season, and positive meridional and vertical advection in autumn (Fig. 11a). The weakened SASM
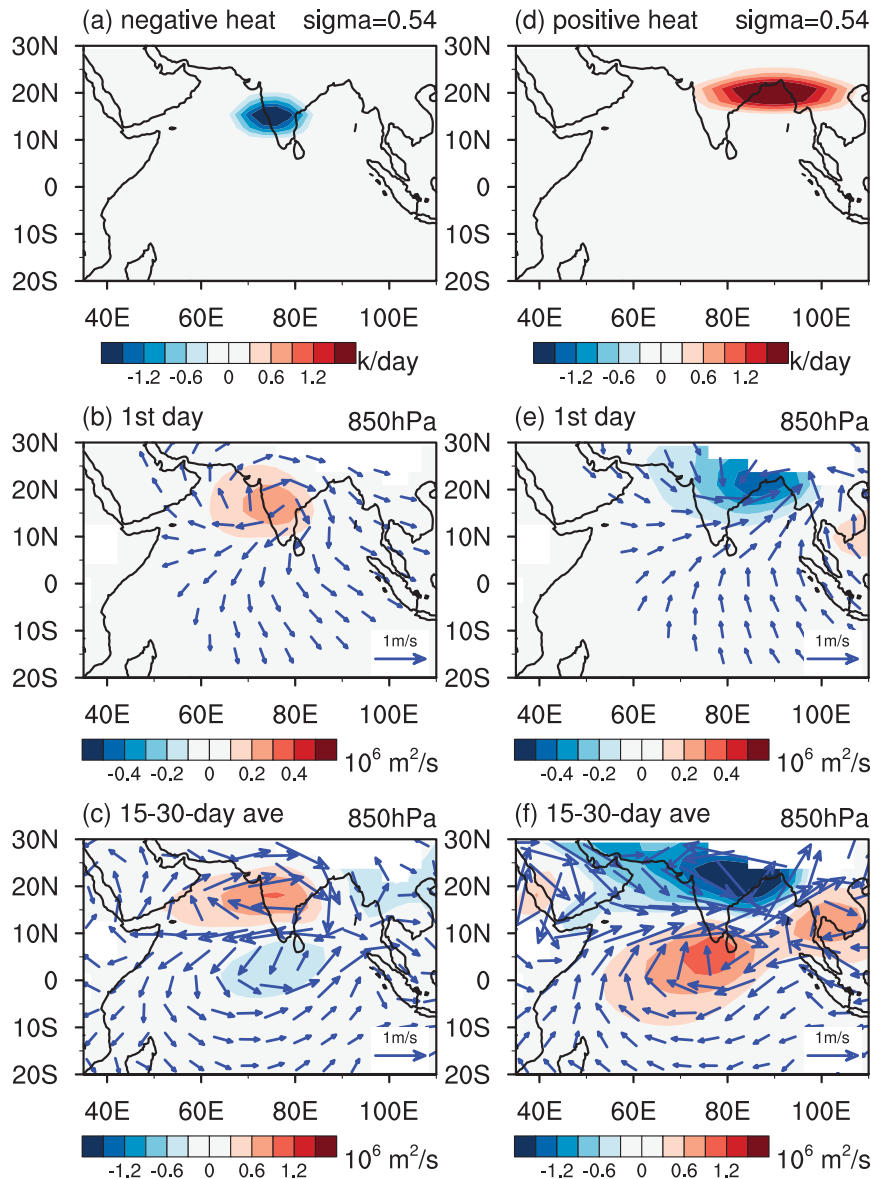
FIG. 8. (a) Spatial distribution of a weak SASM-related diabatic heating source over South Asia at the sigma level of 0.54 in the linear baroclinic model. (b) Response of 850-hPa streamfunction (shading, unit: 10^6 m^2 s^{-1}) and 850-hPa wind (blue vectors, unit: m s^{-1}) to the heating source in (a) on day 1 of the simulation; (c) as in (b), but for values averaged over days 15–30; (d)–(f) as in (a)–(c), but for a strong SASM-related diabatic heating source over South Asia. Only wind vectors >0.02 m s^{-1} are shown.

contributes to surface warming of the western Indian Ocean, which plays a key role in the formation of type W IODs.

For type E IODs, the negative forcing exists between July and mid-September. This is a result of negative surface heat flux, meridional advection, and vertical advection in the western TIO (Fig. 11b) and is consistent with a strong SASM (Fig. 3g). The positive zonal advection associated with the equatorial easterly wind anomaly develops during July–December (Fig. 11b). Positive forcing and warm MLT anomalies exist

during October–December owing to the positive 3D oceanic heat advection (Figs. 10b and 11b). For type C, the weak positive forcing in the western pole oscillates after June. The positive vertical and meridional advections contribute to warming after September, which continues until the end of the year (Fig. 11c). Unlike type E IODs, the insignificant SASM associated with type C IODs leads to the absence of significant negative forcing during the summer monsoon season (Figs. 11b,c). Relatively warm SSTAs are generated in autumn
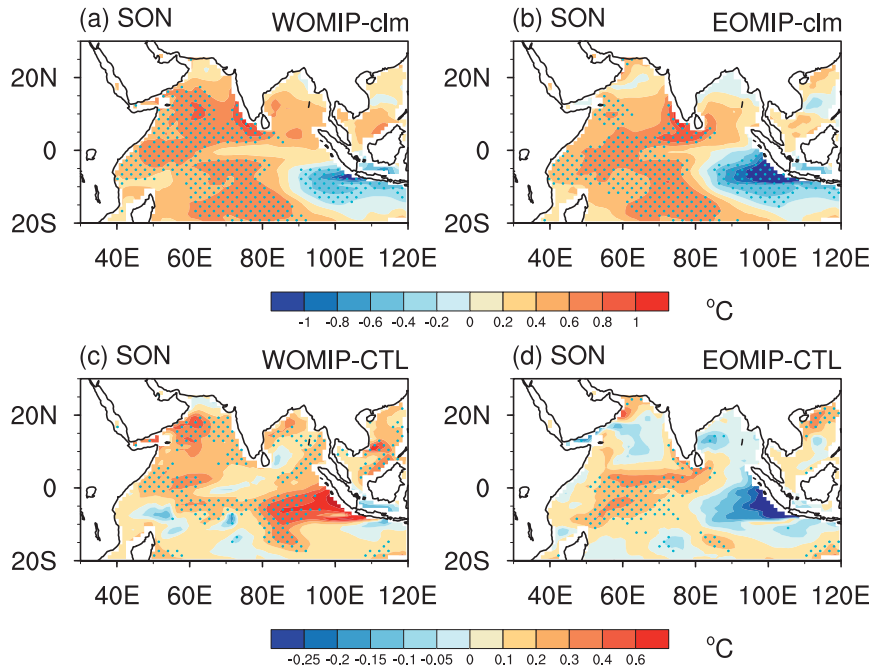
FIG. 9. (a) Ensemble means of SON-averaged SSTAs (unit: °C) of WOMIP experiments relative to the climate mean state of OMIP experiments. (b) As in (a), but for EOMIP experiments. (c) Ensemble means of SON-averaged SST differences (unit: °C) between WOMIP and CTL experiments; they indicate effects of a weak SASM. (d) As (c), but for EOMIP experiments; they indicate effects of a strong SASM. Cyan stippling indicates the 90% confidence level.

(Figs. 3h,l). Surface heat flux dominates the formation of warm MLT anomalies in the western Indian Ocean for type W IODs. Oceanic processes are essential for the warming of the western pole in all three types of IODs, and the warming of the western pole occurs earliest in type W IODs.

2) THE EASTERN POLE

For all three types of positive IODs, the cooling in the mixed layer of the eastern pole is driven by negative 3D oceanic advections after August (Figs. 11d–f). The positive surface heat flux tends to restrict cooling owing to the remarkable positive downward shortwave radiation flux after September (not shown); this is consistent with previous findings that suggested that damping of the eastern pole is associated primarily with surface heat flux (Li et al. 2002; Sun et al. 2014). There are large variations in the amplitude and establishment time of southeasterly wind anomalies off Sumatra (Fig. 3), which give rise to large variations in the development time and intensity of negative forcing over the eastern pole (Figs. 10d–f and 11d–f). For type W IODs, weak southeasterly wind anomalies off Sumatra lead to weak negative oceanic advections. Of three types of IODs, the negative forcing and temperature tendency appear latest in type W and also last for the shortest time, that is, only from mid-July to late September (Figs. 3a–d, 10d, and 11d). This means that the weakest negative MLT anomalies are generated during the IOD mature phase (Figs. 10d–f). In contrast, the strong

negative forcing of type E, which is associated with strong southeasterly wind anomalies off Sumatra, develops significantly between March and the end of September, and especially during July–September (Figs. 3f–h, 10e, and 11e). Strong negative MLT anomalies peak in September (Fig. 10e). For type C IODs, the negative forcing from mid-July to mid-November is slightly weaker than that in type E; this is because of the weaker oceanic processes associated with weaker southeasterly wind anomalies off Sumatra (Figs. 3f–h,j–l, 10e–f, and 11e–f), as indicated by Chen et al. (2016a). In summary, of three types of IODs, the negative MLT anomalies over the eastern pole are the strongest (weakest) in type E (type W) IODs. Although only the positive IOD years during 1980–2017 are used for composite analysis in the mixed layer heat budget, these results are in accord with those from analysis in section 4. The results are insensitive to cases.

6. Discussion

Previous studies indicated that positive IODs generally favor the high Indian summer monsoon rainfall (Ashok et al. 2001; Hrudya et al. 2020). Because IOD events develop in summer and mature in autumn, it was unclear whether the IOD development is influenced by the SASM. In this study, we analyzed local circulation and subsurface variations of three types of positive IODs, emphasizing the role of different
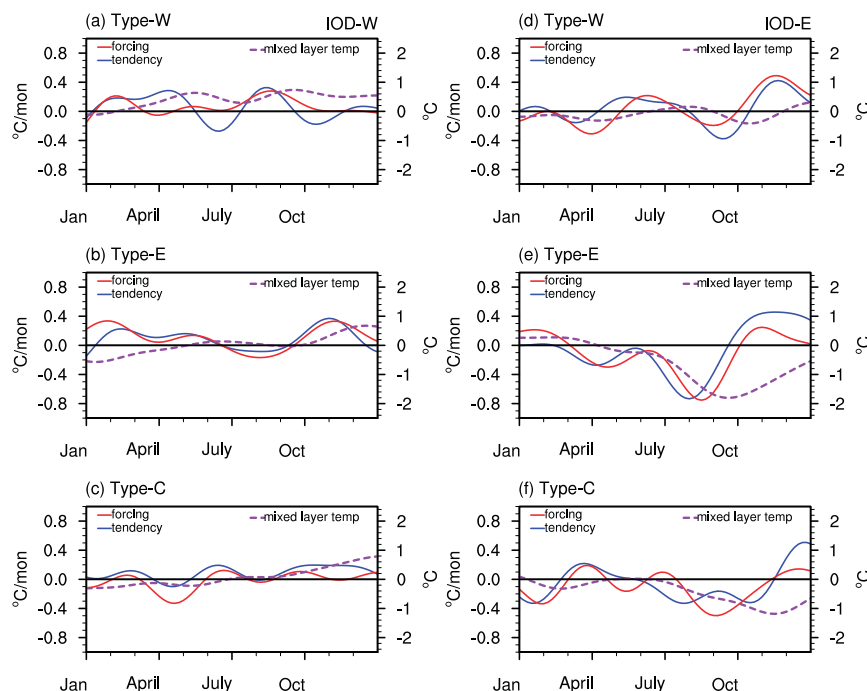
FIG. 10. Composites of mixed layer heat budget closure (left axis) and mixed layer temperature anomalies (right axis) of positive IODs of (top) type W (including 1987 and 2015), (middle) type E (including 1994 and 2006), and (bottom) type C (including 1982, 1997, and 2002) during 1980–2017. Blue solid lines represent mixed layer temperature tendency (unit: °C month^{-1}), i.e., the left side of Eq. (2). Red solid lines represent the forcing (unit: °C month^{-1}) defined as the sum of the first four terms on the right side of Eq. (2), i.e., net surface heat flux, zonal advection, meridional advection, and vertical advection. Purple dashed lines represent mixed layer temperature anomalies (unit: °C). Results are (a)–(c) area-averaged values for the western pole of the IOD (IOD-W) and (d)–(f) area-averaged values for the eastern pole of the IOD (IOD-E). Results are from the pentad dataset with 18–657-pentad (3–108 month) bandpass filtering.

SASM anomalies in modulating the SSTA pattern during IOD development. Examination of triggers of different types of IODs lies outside the scope of the present study but deserves further research.

Large-scale tropical atmosphere circulations are dynamically associated with each other. It is possible that El Niño plays an important role in the formation of type W and type C IODs. Type W IODs always co-occur with El Niño (Table 1); this could be a result of the remote forcing of El Niño via large-scale circulation changes (Fan et al. 2017). The establishment of easterly wind anomalies in the equatorial Indian Ocean is closely related to warm SSTAs in the equatorial eastern Pacific Ocean before April (Fig. S4a). Equatorial zonal wind anomalies could contribute to warming in the southwestern TIO through the westward propagation of downwelling Rossby waves, favoring the weakening of the SASM during May–June (Figs. 3a,b, 6a,b). Moreover, El Niño can also directly contribute to the weakening of the SASM through its effects on the Walker circulation (Fan et al. 2021).

Type C IODs also co-occur with El Niño but without an obvious SASM signal. Warm SSTAs start to develop in the northeastern Pacific Ocean in the absence of extremely

significant easterly wind anomalies in the equatorial Indian Ocean during March–April (Figs. 3i and S4i). Along with strengthening of warm SSTAs in the eastern equatorial Pacific, the significant cold SSTAs and depressed convection over the Maritime Continent become established during July–August (Figs. 3k, 4h, and S4k). On the basis of their numerical modeling study, Li et al. (2003) claimed that El Niño influences the IOD primarily via changes in the intensity of the Indian monsoon and the convection over the Maritime Continent. We speculate that type W and type C IODs might be dominated by these processes, respectively, whereas most type E IODs are independent of El Niño (Table 1). Positive type E IODs co-occurred with El Niño in 1994 and 2006. Warm SSTAs in the tropical eastern Pacific develop later in the two years than in other IOD co-occurring with El Niño years and have little effect in triggering the IODs (Figs. S4e–h). Fan et al. (2017) attributed the year of 2006 to an autumn-type El Niño, which has no direct influence on the development of positive IODs. Thus, we speculate that the triggering mechanism of type E IODs might be related more to local air–sea interactions, such as anomalous cross-equatorial flow (Fischer et al. 2005; Guo et al. 2015), than to El Niño. This is consistent with the earlier view that the
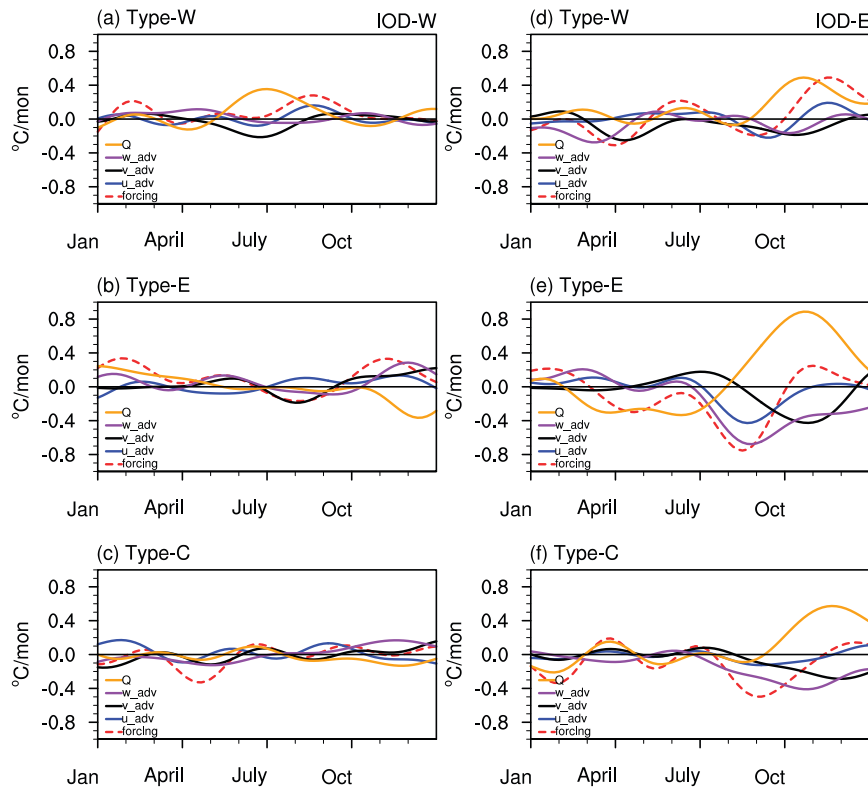
FIG. 11. Composites of the forcing (red dashed lines; unit: $^{\circ}$C month^{-1}) defined as the sum of the first four terms on the right side of Eq. (2), i.e., the sum of net surface heat flux (orange solid lines), zonal advection (blue solid lines), meridional advection (black solid lines), and vertical advection (purple solid lines) of positive IODs of (top) type W, (middle) type E, and (bottom) type C during 1980–2017. (a)–(c) Are area-averaged values for the western pole of the IOD (IOD-W). (d)–(f) The eastern pole of the IOD (IOD-E). Results are from the pentad dataset with 18–657-pentad (3–108-month) bandpass filtering.

eastern pole is more prominent during independent IOD events (Drbohlav et al. 2007; Hong et al. 2008b), and that warm SSTAs of the western pole tend to be slightly stronger for IODs related to ENSO than for independent IODs (Behera et al. 2006; Zhang et al. 2019).

As highlighted by G. Huang et al. (2010), SSTA patterns in the TIO can have diverse impacts on regional climate. Thus, the SSTA development over the TIO in the season that follows IOD events and variations associated with the IOD type also deserve further investigation. Previous studies demonstrated that the Indian Ocean basin mode is highly related to the ENSO (Yang et al. 2007; Xie et al. 2009; Wu et al. 2010). Our results show that the Indian Ocean basin mode was not triggered when type E IODs co-occur with El Niño, such as in 1994 and 2006 (Figs. 12e–h). For years in which type W and type C IODs co-occur with El Niño, there is significant warming in the TIO in the winter and spring following the IOD events (Figs. 12a–d,i–l). These results suggest the importance of western pole warming in the establishment of the positive Indian Ocean basin mode. The correlation coefficient between the autumn SSTA in the western pole and the Indian Ocean basin mode index of the winter (spring) following the

IOD event is 0.75 (0.59); this is much higher than −0.33 (−0.26), which is the value of the same coefficient but for the eastern pole. Different IODs may exert disparate influences on warming across the TIO basin.

Moreover, warm SSTAs during the winter and spring following type W IOD events contribute to strengthening the cross-equatorial flow off East Africa in the early summer following the event (Figs. 12a–d). Conversely, the warm SSTAs are significantly stronger in the south than in the north of the Indian Ocean during the winter and early spring following type C IODs and favor the weakening of the cross-equatorial flow off East Africa (Figs. 12i–l).

7. Summary

In this study, to investigate the relationship between IODs and the SASM and the appearance of TIO basin warming following IOD events, IOD events were classified as type W (type E) if the SSTA amplitude of the western (eastern) pole exceeds twice that in the eastern (western) pole; otherwise, IODs were classified as type C.
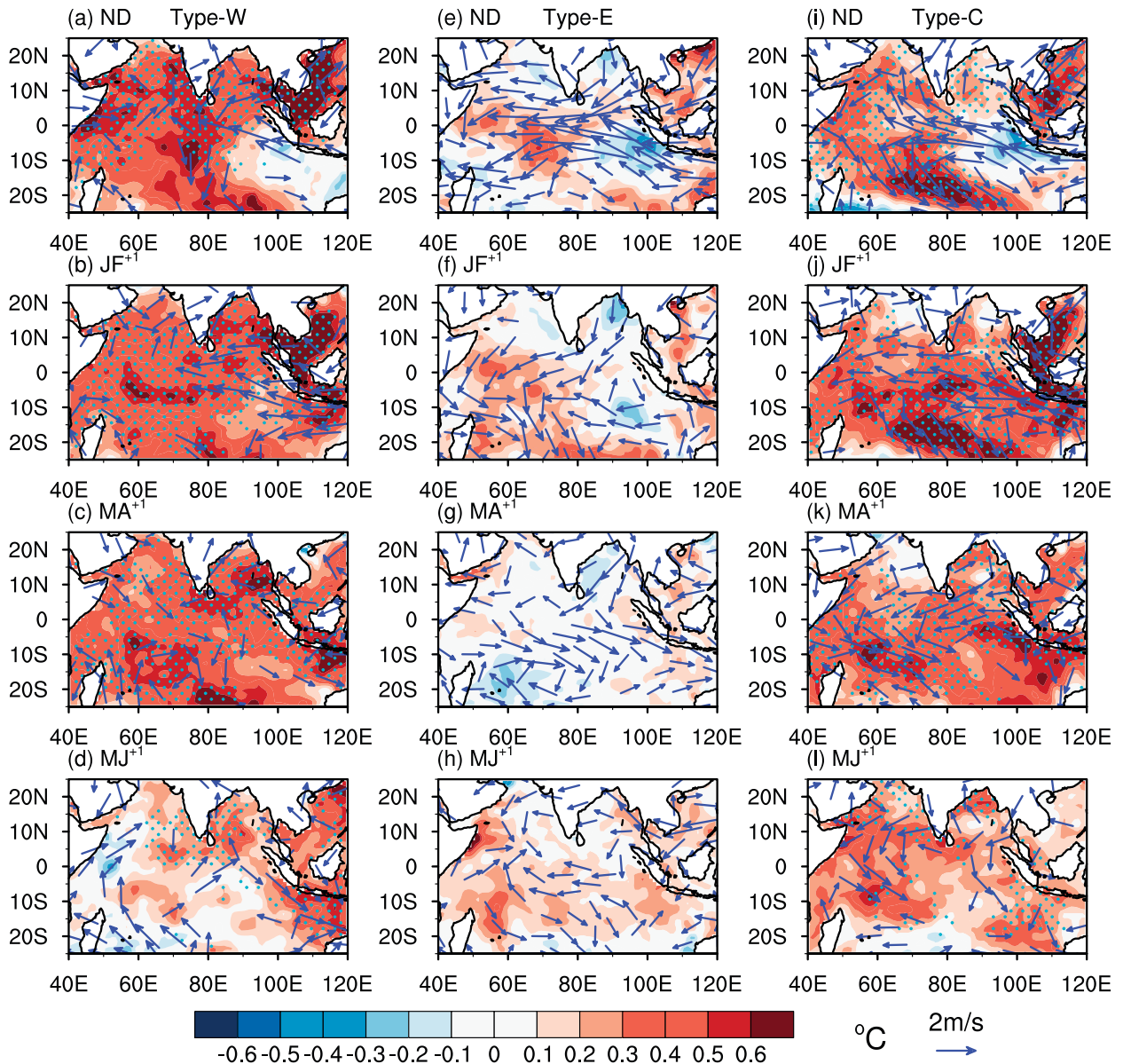
FIG. 12. As in Fig. 3, but for (a),(e),(i) November–December (ND) of the years in which IODs co-occur with El Niño; (b),(f),(j) January–February in the year following the IOD event (JF^{+1}); (c),(g),(k) March–April in the year following the IOD event (MA^{+1}); (d),(h),(l) May–June in the year following the IOD event (MJ^{+1}). Cyan stippling in (a)–(d) and (i)–(l) indicates the 90% confidence level. Only wind vectors that are significant at the 90% confidence level in (a)–(d) and (i)–(l) are shown. Only wind vectors > 0.5 m s^{-1} in (e)–(h) are shown.

Type W positive IODs are associated with a weak South Asian high and SASM from May into summer. The weakening of the SASM induces significant warming of the western pole via reduced WES feedback and coastal upwelling. The significant east–west SST gradient promotes development of southeasterly wind anomalies off Sumatra during September–October, and weak cold SSTAs in the eastern pole. The warming of the western pole is significantly stronger than the cooling of the eastern pole during May–December. For type E

IODs, intensification of both the South Asian high and the SASM results in feeble warming of the western pole. Meanwhile, interactions among strong SASM wind anomalies, strong convection over South Asia and cold SSTAs of the eastern pole in summer contribute to cold SSTAs in the eastern pole during the IOD mature phase. The eastern pole cooling is significantly stronger than the western pole warming during the mature phase. For type C IODs, cold SSTAs in the eastern pole and warm SSTAs in the western

pole develop synchronously without obvious SASM anomalies and achieve almost the same intensity during the mature phase.

Different atmospheric circulations associated with three types of IODs induce different subsurface temperature and thermocline anomalies. The positive subsurface dipole in type W IODs develops early around March–April, while the positive subsurface dipole in type E IODs results from the translation of the negative subsurface dipole. The subsurface dipole of type C IODs develops from the eastern pole, with the warming of the western pole occurring in September–October.

Analysis of the mixed layer heat budget equation indicates that of three types of IODs, warm MLT anomalies in the western pole begin developing earliest and subsequently become strongest during the mature phase in type W IODs; this begins in early spring and is a result of positive zonal advection and surface heat flux. Type E, which is the weakest type of IODs in the western Indian Ocean, and type C IODs are both influenced by positive 3D oceanic heat advections. Cold MLT anomalies of the eastern pole result from negative 3D oceanic heat advections during three types of IOD development. Surface heat flux tends to limit cooling of the eastern pole after September. Of three types of IODs, the development of cold MLT anomalies in the eastern pole is the weakest in type W and the strongest during the type E IOD mature phase.

The IOD is an important coupled ocean–atmosphere mode in the TIO, with surface wind anomalies playing a crucial role in its development stage. However, clear characterization of the relationship between the SASM and IOD is missing from previous studies. In this study, we put forth a comprehensive classification system of IODs based on differences between SSTA amplitude of the eastern and western pole of the IOD. This classification allows clear identification of evolution features and dynamics of different types of IODs and highlights the influence of SASM anomalies on IOD type. Observation data are in close agreement with model simulation results. Our results also will contribute to predictions of regional climate following IOD events. Interestingly, our further analysis (not shown) suggests that the latest extreme positive IOD in the year of 2019 (Du et al. 2020; Lu and Ren 2020) belongs to type C IOD, accompanied by a weakened SASM in May–June and a reinforced SASM in July–September (Gadgil et al. 2019; Ratna et al. 2021; Cherchi et al. 2021). The evolution of the SSTAs in the western and eastern pole analogously appears to reflect the role of SASM in modulating SSTA patterns. We note, however, that despite these instructive classifications, each individual event is unique in their own right, and the associated mechanisms may evolve in the backdrop of a changing climate (e.g., Wang et al. 2020). Further, owing to the strong air–sea interactions over the Indian Ocean, the role of the SASM in modulating the SSTA pattern during IOD development should be verified using an air–sea coupled model in the future.

REFERENCES

Anil, N., M. R. R. Kumar, R. Sajeev, and P. K. Saji, 2016: Role of distinct flavours of IOD events on Indian summer monsoon. *Nat. Hazards*, **82**, 1317–1326, https://doi.org/10.1007/s11069-016-2245-9.

Annamalai, H., R. Murtugudde, J. Potemra, S. P. Xie, P. Liu, and B. Wang, 2003: Coupled dynamics over the Indian Ocean: Spring initiation of the zonal mode. *Deep-Sea Res. II*, **50**, 2305–2330, https://doi.org/10.1016/S0967-0645(03)00058-4.

Ashfaq, M., Y. Shi, W. W. Tung, R. J. Trapp, X. J. Gao, J. S. Pal, and N. S. Diffenbaugh, 2009: Suppression of South Asian summer monsoon precipitation in the 21st century. *Geophys. Res. Lett.*, **36**, L01704, https://doi.org/10.1029/2008GL036500.

Ashok, K., Z. Y. Guan, and T. Yamagata, 2001: Impact of the Indian Ocean dipole on the relationship between the Indian monsoon rainfall and ENSO. *Geophys. Res. Lett.*, **28**, 4499–4502, https://doi.org/10.1029/2001GL013294.

——, ——, and ——, 2003: A look at the relationship between the ENSO and the Indian Ocean dipole. *J. Meteor. Soc. Japan*, **81**, 41–56, https://doi.org/10.2151/jmsj.81.41.

Balmaseda, M. A., K. Mogensen, and A. T. Weaver, 2013: Evaluation of the ECMWF ocean reanalysis system ORAS4. *Quart. J. Roy. Meteor. Soc.*, **139**, 1132–1161, https://doi.org/10.1002/qj.2063.

Behera, S. K., J. J. Luo, S. Masson, S. A. Rao, H. Sakum, and T. Yamagata, 2006: A CGCM study on the interaction between IOD and ENSO. *J. Climate*, **19**, 1688–1705, https://doi.org/10.1175/JCLI3797.1.

Behringer, D. W., and Y. Xue, 2004: Evaluation of the global ocean data assimilation system at NCEP: The Pacific Ocean. *Eighth Symp. on Integrated Observing and Assimilation Systems for Atmosphere, Oceans, and Land Surface*, Seattle, WA, Amer. Meteor. Soc., 2.3, https://ams.confex.com/ams/pdfpapers/70720.pdf.

Birkett, C., R. Murtugudde, and T. Allan, 1999: Indian Ocean climate event brings floods to East Africa's lakes and the Sudd Marsh. *Geophys. Res. Lett.*, **26**, 1031–1034, https://doi.org/10.1029/1999GL900165.

Cai, W. J., X. T. Zheng, E. Weller, M. Collins, T. Cowan, M. Lengaigne, W. D. Yu, and T. Yamagata, 2013: Projected response of the Indian Ocean dipole to greenhouse warming. *Nat. Geosci.*, **6**, 999–1007, https://doi.org/10.1038/ngeo2009.

——, A. Santoso, G. J. Wang, E. Weller, L. X. Wu, K. Ashok, Y. Masumoto, and T. Yamagata, 2014: Increased frequency of extreme Indian Ocean dipole events due to greenhouse warming. *Nature*, **510**, 254–258, https://doi.org/10.1038/nature13327.

——, K. Yang, L. X. Wu, G. Huang, A. Santoso, N. Benjamin, G. J. Wang, and T. Yamagata, 2020: Opposite response of strong and moderate positive Indian Ocean dipole to global warming. *Nat. Climate Change*, **11**, 27–32, https://doi.org/10.1038/s41558-020-00943-1.

Carton, J. A., and B. S. Giese, 2008: A reanalysis of ocean climate using Simple Ocean Data Assimilation (SODA). *Mon. Wea. Rev.*, **136**, 2999–3017, https://doi.org/10.1175/2007MWR1978.1.

Chen, G. X., W. Q. Han, Y. L. Li, D. X. Wang, and M. J. McPhaden, 2015: Seasonal-to-interannual time-scale dynamics of the equatorial undercurrent in the Indian Ocean. *J. Phys. Oceanogr.*, **45**, 1532–1553, https://doi.org/10.1175/JPO-D-14-0225.1.

——, ——, ——, and ——, 2016a: Interannual variability of equatorial eastern Indian Ocean upwelling: Local versus remote forcing. *J. Phys. Oceanogr.*, **46**, 789–807, https://doi.org/10.1175/JPO-D-15-0117.1.

——, ——, Y. Q. Shu, Y. L. Li, D. X. Wang, and Q. Xie, 2016b: The role of equatorial undercurrent in sustaining the eastern Indian Ocean upwelling. *Geophys. Res. Lett.*, **43**, 6444–6451, https://doi.org/10.1002/2016GL069433.

Cherchi, A., P. Terray, S. B. Ratna, S. Sankar, K. P. Sooraj, and S. Behera, 2021: Indian Ocean dipole influence on Indian summer monsoon and ENSO: A review. *Indian Summer Monsoon Variability, El-Niño Teleconnections and Beyond*, Elsevier, 157–182, https://doi.org/10.1016/B978-0-12-822402-1.00011-9.

Cui, Y. F., A. M. Duan, Y. M. Liu, and G. X. Wu, 2015: Interannual variability of the spring atmospheric heat source over the Tibetan Plateau forced by the North Atlantic SSTA. *Climate Dyn.*, **45**, 1617–1634, https://doi.org/10.1007/s00382-014-2417-9.

Dong, S., S. T. Gille, and J. Sprintall, 2007: An assessment of the Southern Ocean mixed layer heat budget. *J. Climate*, **20**, 4425–4442, https://doi.org/10.1175/JCLI4259.1.

Drbohlav, H. K. L., S. Gualdi, and A. Navarra, 2007: A diagnostic study of the Indian Ocean dipole mode in El Niño and non–El Niño years. *J. Climate*, **20**, 2961–2977, https://doi.org/10.1175/JCLI4153.1.

Du, Y., T. D. Qu, G. Meyers, Y. Masumoto, and H. Sasaki, 2005: Seasonal heat budget in the mixed layer of the southeastern tropical Indian Ocean in a high-resolution ocean general circulation model. *J. Geophys. Res.*, **110**, C04012, https://doi.org/10.1029/2004JC002845.

——, W. J. Cai, and Y. L. Wu, 2013: A new type of the Indian Ocean dipole since the mid-1970s. *J. Climate*, **26**, 959–972, https://doi.org/10.1175/JCLI-D-12-00047.1.

——, Y. H. Zhang, L. Y. Zhang, T. Tozuka, B. Ng, and W. J. Cai, 2020: Thermocline warming induced extreme Indian Ocean dipole in 2019. *Geophys. Res. Lett.*, **47**, e2020GL090079, https://doi.org/10.1029/2020GL090079.

Effy, J. B., P. Francis, S. Ramakrishna, and A. Mukherjee, 2020: Anomalous warming of the western equatorial Indian Ocean in 2007: Role of ocean dynamics. *Ocean Modell.*, **147**, 101542, https://doi.org/10.1016/j.ocemod.2019.101542.

Endo, S., and T. Tozuka, 2016: Two flavors of the Indian Ocean dipole. *Climate Dyn.*, **46**, 3371–3385, https://doi.org/10.1007/s00382-015-2773-0.

Fan, F. X., R. P. Lin, X. H. Fang, F. Xue, F. Zheng, and J. Zhu, 2021: Influence of the eastern Pacific and central Pacific types of ENSO on the South Asian summer monsoon. *Adv. Atmos. Sci.*, **38**, 12–28, https://doi.org/10.1007/s00376-020-0055-1.

Fan, L., Q. Y. Liu, C. Z. Wang, and F. Y. Guo, 2017: Indian Ocean dipole modes associated with different types of ENSO development. *J. Climate*, **30**, 2233–2249, https://doi.org/10.1175/JCLI-D-16-0426.1.

Fischer, A. S., P. Terray, E. Guilyardi, S. Gualdi, and P. Delecluse, 2005: Two independent triggers for the Indian Ocean dipole/zonal mode in a coupled GCM. *J. Climate*, **18**, 3428–3449, https://doi.org/10.1175/JCLI3478.1.

Gadgil, S., P. A. Francis, and P. N. Vinayachandran, 2019: Summer monsoon of 2019: Understanding the performance so far and speculating about the rest of the season. *Curr. Sci.*, **117**, 783–793, https://doi.org/10.18520/cs/v117/i5/783-793.

Guo, F. Y., Q. Y. Liu, S. Sun, and J. L. Yang, 2015: Three types of Indian Ocean dipoles. *J. Climate*, **28**, 3073–3092, https://doi.org/10.1175/JCLI-D-14-00507.1.

——, ——, J. L. Yang, and L. Fan, 2018: Three types of Indian Ocean basin modes. *Climate Dyn.*, **51**, 4357–4370, https://doi.org/10.1007/s00382-017-3676-z.

He, B., Y. M. Liu, G. X. Wu, Z. Q. Wang, and Q. Bao, 2019: The role of air–sea interactions in regulating the thermal effect of the Tibetan–Iranian Plateau on the Asian summer monsoon. *Climate Dyn.*, **52**, 4227–4245, https://doi.org/10.1007/s00382-018-4377-y.

Hong, C. C., T. Li, and J. J. Luo, 2008a: Asymmetry of the Indian Ocean dipole. Part II: Model diagnosis. *J. Climate*, **21**, 4849–4858, https://doi.org/10.1175/2008JCLI2223.1.

——, M. M. Lu, and M. Kanamitsu, 2008b: Temporal and spatial characteristics of positive and negative Indian Ocean dipole with and without ENSO. *J. Geophys. Res.*, **113**, D08107, https://doi.org/10.1029/2007JD009151.

——, T. Li, L. Ho, and J. S. Kug, 2008c: Asymmetry of the Indian Ocean dipole. Part I: Observational analysis. *J. Climate*, **21**, 4834–4848, https://doi.org/10.1175/2008JCLI2222.1.

Hrudya, P., H. Varikoden, and R. Vishnu, 2020: A review on the Indian summer monsoon rainfall, variability and its association with ENSO and IOD. *Meteor. Atmos. Phys.*, **133**, 1–14, https://doi.org/10.1007/s00703-020-00734-5.

Huang, B. H., and J. Shukla, 2007: Mechanisms for the interannual variability in the tropical Indian Ocean. Part II: Regional processes. *J. Climate*, **20**, 2937–2960, https://doi.org/10.1175/JCLI4169.1.

Huang, B. Y., Y. Xue, D. X. Zhang, A. Kumar, and M. J. McPhaden, 2010: The NCEP GODAS ocean analysis of the tropical Pacific mixed layer heat budget on seasonal to interannual time scales. *J. Climate*, **23**, 4901–4925, https://doi.org/10.1175/2010JCLI3373.1.

Huang, G., K. M. Hu, and S. P. Xie, 2010: Strengthening of tropical Indian Ocean teleconnection to the northwest Pacific since the mid-1970s: An atmospheric GCM study. *J. Climate*, **23**, 5294–5304, https://doi.org/10.1175/2010JCLI3577.1.

Kalnay, E., and Coauthors, 1996: The NCEP/NCAR 40-Year Reanalysis Project. *Bull. Amer. Meteor. Soc.*, **77**, 437–471, https://doi.org/10.1175/1520-0477(1996)077<0437:TNYRP>2.0.CO;2.

Kobayashi, S., and Coauthors, 2015: The JRA-55 reanalysis: General specifications and basic characteristics. *J. Meteor. Soc. Japan*, **93**, 5–48, https://doi.org/10.2151/jmsj.2015-001.

Krishnan, R., and P. Swapna, 2009: Significant influence of the boreal summer monsoon flow on the Indian Ocean response during dipole events. *J. Climate*, **22**, 5611–5634, https://doi.org/10.1175/2009JCLI2176.1.

Kumar, B. P., J. Vialard, M. Lengaigne, V. S. N. Murty, and M. J. McPhaden, 2012: TropFlux: Air–sea fluxes for the global tropical oceans—Description and evaluation. *Climate Dyn.*, **38**, 1521–1543, https://doi.org/10.1007/s00382-011-1115-0.

——, ——, ——, ——, ——, M. F. Cronin, F. Pinsard, and K. G. Reddy, 2013: TropFlux wind stresses over the tropical oceans: Evaluation and comparison with other products. *Climate Dyn.*, **40**, 2049–2071, https://doi.org/10.1007/s00382-012-1455-4.

Large, W. G., and S. G. Yeager, 2004: Diurnal to decadal global forcing for ocean and sea-ice models: The data sets and flux climatologies. NCAR Tech. Note NCAR/TN-460+STR, 105 pp., https://doi.org/10.5065/D6KK98Q6.

Latif, M., D. Dommenget, M. Dima, and A. Grotzner, 1999: The role of Indian Ocean sea surface temperature in forcing east African rainfall anomalies during December–January 1997/98. *J. Climate*, **12**, 3497–3504, https://doi.org/10.1175/1520-0442(1999)012<3497:TROIOS>2.0.CO;2.

Lestari, D. O., E. Sutriyono, and I. Sabaruddin, 2018: Severe drought event in Indonesia following 2015/16 El Niño/

positive Indian dipole events. *J. Phys. Conf. Ser.*, **1011**, 012040, https://doi.org/10.1088/1742-6596/1011/1/012040.

Li, J. P., and Q. C. Zeng, 2002: A unified monsoon index. *Geophys. Res. Lett.*, **29**, 111–115, https://doi.org/10.1029/2001GL013874.

Li, T., Y. S. Zhang, E. Lu, and D. L. Wang, 2002: Relative role of dynamic and thermodynamic processes in the development of the Indian Ocean dipole: An OGCM diagnosis. *Geophys. Res. Lett.*, **29**, 251–254, https://doi.org/10.1029/2002GL015789.

——, B. Wang, C. P. Chang, and Y. S. Zhang, 2003: A theory for the Indian Ocean dipole-zonal mode. *J. Atmos. Sci.*, **60**, 2119–2135, https://doi.org/10.1175/1520-0469(2003)060<2119:ATFTIO>2.0.CO;2.

Liebmann, B., and C. A. Smith, 1996: Description of a complete (interpolated) outgoing longwave radiation dataset. *Bull. Amer. Meteor. Soc.*, **77**, 1275–1277, https://doi.org/10.1175/1520-0477(1996)077<1255:EA>2.0.CO;2.

Lin, P., and Coauthors, 2020: LICOM model datasets for the CMIP6 ocean model intercomparison project. *Adv. Atmos. Sci.*, **37**, 239–249, https://doi.org/10.1007/s00376-019-9208-5.

Liu, B. Q., Y. M. Liu, G. X. Wu, J. H. Yan, J. H. He, and S. L. Ren, 2014: Asian summer monsoon onset barrier and its formation mechanism. *Climate Dyn.*, **45**, 711–726, https://doi.org/10.1007/s00382-014-2296-0.

——, C. W. Zhu, and Y. Yuan, 2017: Two interannual dominant modes of the South Asian high in May and their linkage to the tropical SST anomalies. *Climate Dyn.*, **49**, 2705–2720, https://doi.org/10.1007/s00382-016-3490-z.

Liu, L., G. Yang, X. Zhao, L. Feng, G. Q. Han, Y. Wu, and W. D. Yu, 2017: Why was the Indian Ocean dipole weak in the context of the extreme El Niño in 2015? *J. Climate*, **30**, 4755–4761, https://doi.org/10.1175/JCLI-D-16-0281.1.

Liu, Q. Y., M. Feng, D. X. Wang, and S. Wijffels, 2015: Interannual variability of the Indonesian throughflow transport: A revisit based on 30 year expendable bathythermograph data. *J. Geophys. Res. Oceans*, **120**, 8270–8282, https://doi.org/10.1002/2015JC011351.

Liu, Y. M., B. Hoskins, and M. Blackburn, 2007: Impact of Tibetan orography and heating on the summer flow over Asia. *J. Meteor. Soc. Japan*, **85B**, 1–19, https://doi.org/10.2151/jmsj.85B.1.

Loschnigg, J., G. A. Meehl, P. J. Webster, J. M. Arblaster, and G. P. Compo, 2003: The Asian monsoon, the tropospheric biennial oscillation, and the Indian Ocean zonal mode in the NCAR CSM. *J. Climate*, **16**, 1617–1642, https://doi.org/10.1175/1520-0442(2003)016<1617:TAMTTB>2.0.CO;2.

Lu, B., and H. L. Ren, 2020: What caused the extreme Indian Ocean dipole event in 2019? *Geophys. Res. Lett.*, **47**, e2020GL087768, https://doi.org/10.1029/2020GL087768.

Luo, J. J., R. C. Zhang, S. K. Behera, Y. Masumoto, F. F. Jin, R. Lukas, and T. Yamagata, 2010: Interaction between El Niño and extreme Indian Ocean dipole. *J. Climate*, **23**, 726–742, https://doi.org/10.1175/2009JCLI3104.1.

Mao, J. Y., and M. Wang, 2018: The 30–60-day intraseasonal variability of sea surface temperature in the South China Sea during May–September. *Adv. Atmos. Sci.*, **35**, 550–566, https://doi.org/10.1007/s00376-017-7127-x.

Murtugudde, R., J. P. McCreary, and A. J. Busalacchi, 2000: Oceanic processes associated with anomalous events in the Indian Ocean with relevance to 1997–1998. *J. Geophys. Res.*, **105**, 3295–3306, https://doi.org/10.1029/1999JC900294.

Nur'utami, M. N., and R. Hidayat, 2016: Influences of IOD and ENSO to Indonesian rainfall variability: Role of atmosphere-

ocean interaction in the Indo-Pacific sector. *Procedia Environ. Sci.*, **33**, 196–203, https://doi.org/10.1016/j.proenv.2016.03.070.

Ogata, T., S. P. Xie, J. Lan, and X. T. Zheng, 2013: Importance of ocean dynamics for the skewness of the Indian Ocean dipole mode. *J. Climate*, **26**, 2145–2159, https://doi.org/10.1175/JCLI-D-11-00615.1.

Paulson, C. A., and J. J. Simpson, 1977: Irradiance measurements in the upper ocean. *J. Phys. Oceanogr.*, **7**, 952–956, https://doi.org/10.1175/1520-0485(1977)007<0952:IMITUO>2.0.CO;2.

Rao, S. A., and S. K. Behera, 2005: Subsurface influence on SST in the tropical Indian Ocean: Structure and interannual variability. *Dyn. Atmos. Oceans*, **39**, 103–135, https://doi.org/10.1016/j.dynatmoce.2004.10.014.

——, ——, Y. Masumoto, and T. Yamagata, 2002: Interannual subsurface variability in the tropical Indian Ocean with a special emphasis on the Indian Ocean dipole. *Deep-Sea Res. II*, **49**, 1549–1572, https://doi.org/10.1016/S0967-0645(01)00158-8.

Ratna, S. B., A. Cherchi, T. J. Osborn, M. Joshi, and U. Uppara, 2021: The extreme positive Indian Ocean dipole of 2019 and associated Indian summer monsoon rainfall response. *Geophys. Res. Lett.*, **48**, e2020GL091497, https://doi.org/10.1029/2020GL091497.

Rayner, N. A., D. E. Parker, E. B. Horton, C. K. Folland, L. V. Alexander, D. P. Rowell, E. C. Kent, and A. Kaplan, 2003: Global analyses of sea surface temperature, sea ice, and night marine air temperature since the late nineteenth century. *J. Geophys. Res.*, **108**, 4407, https://doi.org/10.1029/2002JD002670.

Saji, N. H., and T. Yamagata, 2003: Possible impacts of Indian Ocean dipole mode events on global climate. *Climate Res.*, **25**, 151–169, https://doi.org/10.3354/cr025151.

——, B. N. Goswami, P. N. Vinayachandran, and T. Yamagata, 1999: A dipole mode in the tropical Indian Ocean. *Nature*, **401**, 360–363, https://doi.org/10.1038/43854.

Stuecker, M. F., A. Timmermann, F. F. Jin, Y. Chikamoto, W. J. Zhang, A. T. Wittenberg, E. Widiasih, and S. Zhao, 2017: Revisiting ENSO/Indian Ocean dipole phase relationships. *Geophys. Res. Lett.*, **44**, 2481–2492, https://doi.org/10.1002/2016GL072308.

Sun, S. W., Y. Fang, Tana, and B. C. Liu, 2014: Dynamical mechanisms for asymmetric SSTA patterns associated with some Indian Ocean dipoles. *J. Geophys. Res. Oceans*, **119**, 3076–3097, https://doi.org/10.1002/2013JC009651.

——, J. Lan, Y. Fang, Tana, and X. Q. Gao, 2015: A triggering mechanism for the Indian Ocean dipoles independent of ENSO. *J. Climate*, **28**, 5063–5076, https://doi.org/10.1175/JCLI-D-14-00580.1.

Trenberth, K. E., 1997: The definition of El Niño. *Bull. Amer. Meteor. Soc.*, **78**, 2771–2777, https://doi.org/10.1175/1520-0477(1997)078<2771:TDOENO>2.0.CO;2.

Wang, G. J., W. J. Cai, K. Yang, A. Santoso, and T. Yamagata, 2020: A unique feature of the 2019 extreme positive Indian Ocean dipole event. *Geophys. Res. Lett.*, **47**, e2020GL088615, https://doi.org/10.1029/2020GL088615.

Wang, H., R. Murtugudde, and A. Kumar, 2016: Evolution of Indian Ocean dipole and its forcing mechanisms in the absence of ENSO. *Climate Dyn.*, **47**, 2481–2500, https://doi.org/10.1007/s00382-016-2977-y.

Wang, J., and D. L. Yuan, 2015: Roles of western and eastern boundary reflections in the interannual sea level variations during negative Indian Ocean dipole events. *J. Phys. Oceanogr.*, **45**, 1804–1821, https://doi.org/10.1175/JPO-D-14-0124.1.

Wang, X., and C. Z. Wang, 2014: Different impacts of various El Niño events on the Indian Ocean dipole. *Climate Dyn.*, **42**, 991–1005, https://doi.org/10.1007/s00382-013-1711-2.

Watanabe, M., and M. Kimoto, 2000: Atmosphere-ocean thermal coupling in the North Atlantic: A positive feedback. *Quart. J. Roy. Meteor. Soc.*, **126**, 3343–3369, https://doi.org/10.1002/qj.49712657017.

——, and F. F. Jin, 2002: Role of Indian Ocean warming in the development of Philippine Sea anticyclone during ENSO. *Geophys. Res. Lett.*, **29**, 1478, https://doi.org/10.1029/2001GL014318.

Webster, P. J., A. M. Moore, J. P. Loschnigg, and R. R. Leben, 1999: Coupled ocean–atmosphere dynamics in the Indian Ocean during 1997–98. *Nature*, **401**, 356–360, https://doi.org/10.1038/43848.

Wei, W., Y. T. Wu, S. Yang, and W. Zhou, 2019: Role of the South Asian high in the onset process of the Asian summer monsoon during spring-to-summer transition. *Atmosphere*, **10**, 239, https://doi.org/10.3390/atmos10050239.

Wu, B., T. Li, and T. Zhou, 2010: Relative contributions of the Indian Ocean and local SST anomalies to the maintenance of the western North Pacific anomalous anticyclone during the El Niño decaying summer. *J. Climate*, **23**, 2974–2986, https://doi.org/10.1175/2010JCLI3300.1.

Xie, S. P., and S. G. H. Philander, 1994: A coupled ocean-atmosphere model of relevance to the ITCZ in the eastern Pacific. *Tellus*, **46**, 340–350, https://doi.org/10.3402/tellusa.v46i4.15484.

——, H. Annamalai, F. A. Schott, and J. P. McCreary, 2002: Structure and mechanisms of south Indian Ocean climate variability. *J. Climate*, **15**, 864–878, https://doi.org/10.1175/1520-0442(2002)015<0864:SAMOSI>2.0.CO;2.

——, K. M. Hu, J. Hafner, H. Tokinaga, Y. Du, G. Huang, and T. Sampe, 2009: Indian Ocean capacitor effect on Indo-western Pacific climate during the summer following El Niño. *J. Climate*, **22**, 730–747, https://doi.org/10.1175/2008JCLI2544.1.

Yang, J., Q. Liu, S.-P. Xie, Z. Liu, and L. Wu, 2007: Impact of the Indian Ocean SST basin mode on the Asian summer monsoon. *Geophys. Res. Lett.*, **34**, L02708, https://doi.org/10.1029/2006GL028571.

Yu, W., Y. M. Liu, X.-Q. Yang, G. X. Wu, B. He, J. X. Li, and Q. Bao, 2021: Impact of North Atlantic SST and Tibetan Plateau forcing on seasonal transition of springtime South Asian monsoon circulation. *Climate Dyn.*, **56**, 559–579, https://doi.org/10.1007/s00382-020-05491-0.

Yuan, D. L., and H. L. Liu, 2009: Long-wave dynamics of sea level variations during Indian Ocean dipole events. *J. Phys. Oceanogr.*, **39**, 1115–1132, https://doi.org/10.1175/2008JPO3900.1.

Zhang, L. Y., Y. Du, and W. J. Cai, 2018: Low-frequency variability and the unusual Indian Ocean dipole events in 2015 and 2016. *Geophys. Res. Lett.*, **45**, 1040–1048, https://doi.org/10.1002/2017GL076003.

Zhang, W. J., Y. L. Wang, F. F. Jin, M. F. Stuecker, and A. G. Turner, 2015: Impact of different El Niño types on the El Niño/IOD relationship. *Geophys. Res. Lett.*, **42**, 8570–8576, https://doi.org/10.1002/2015GL065703.

Zhang, Y. Z., J. P. Li, J. Q. Xue, J. Feng, Q. Y. Wang, Y. D. Xu, Y. H. Wang, and F. Zheng, 2018: Impact of the South China Sea summer monsoon on the Indian Ocean dipole. *J. Climate*, **31**, 6557–6573, https://doi.org/10.1175/JCLI-D-17-0815.1.

——, ——, ——, F. Zheng, R. G. Wu, K. J. Ha, and J. Feng, 2019: The relative roles of the South China Sea summer monsoon and ENSO in the Indian Ocean dipole development. *Climate Dyn.*, **53**, 6665–6680, https://doi.org/10.1007/s00382-019-04953-4.